Universität Münster

Commissioning a sensor system for wire tension measurements in the CBM TRD

Bachelor thesis
submitted to the

Institut für Kernphysik
Universität Münster

by
Konstantin Baans

September, 2025

First examiner:	Prof. Dr. Anton Andronic
Second examiner:	Apl. Prof. Dr. Christian Klein-Bösing

Day of submission:	3^{th} September, 2025

Declaration of Academic Integrity

I hereby confirm that this thesis, is solely my own work and that I have used no sources or aids other than the ones stated. All passages in my thesis for which other sources, including electronic media, have been used, be it direct quotes or content references, have been acknowledged as such and the sources cited. I am aware that plagiarism is considered an act of deception which can result in sanction in accordance with the examination regulations.
I confirm that I am aware that my work may be cross-checked with other texts to identify possible similarities and that it may be stored in a database for this purpose. I confirm that I have not submitted the following thesis in part or whole as an examination paper before.

Münster, 3th September, 2025

K. Baans

Konstantin Alexander Baans

Contents

Chapter 1

Introduction

The matter in the universe in which we live consists of particles of many various species, which behave and interact by certain fundamental rules. Investigating these rules helps building up an understanding of processes and mechanisms, such as the big bang, that marks the start of the universe we know. One of the most interesting stages of this event is the emergence of what we describe as the quark-gluon plasma (QGP). In this state of matter, the confinement of the quarks that make up hadronic matter such as protons, neutrons and a variety of mesons is canceled so that quarks and gluons (bosons of the strong interaction) can move freely. However, the conditions required for matter to be in such a state are extreme, so that the experiments investigating the QGP need to be of large scales. Today's particle accelerators reach sizes and lengths of multiple kilometers and can provide beam energies of up to several GeV or even TeV.

The research done in this thesis contributes to the development of the Compressed Baryonic Matter (CBM) nuclear experiment, which is part of the Facility for Antiproton and Ion Research (FAIR) in Darmstadt, Germany. It will be connected to the synchrotron SIS100 and is devoted to the investigation of Quantum Chromo-Dynamics (QCD) in the region of high net-baryon densities. This thesis continues the development of a Wire Tension Testing Device (WTTD), which measures the mechanical tension of the electrode wires within Multi Wire Proportional Chambers (MWPC) that are used for particle detection in the Transition Radiation Detector (TRD) of the CBM experiment.

Chapter 2

Experimental background – CBM at FAIR

The QGP was present between just 10^{-10} s and 10^{-6} s after the big bang and dissolved after the hadronization process of the colour-charged particles into bound states [16]. This phase of matter is only present at high temperatures (above 160 MeV [1]) or at high net-baryon densities. As shown in the sketched QCD phase diagram in Figure 2.1, the transition between hadronic matter and the QGP at high temperatures and low net-baryon densities is expected to be a smooth crossover. This section is examined by experiments such

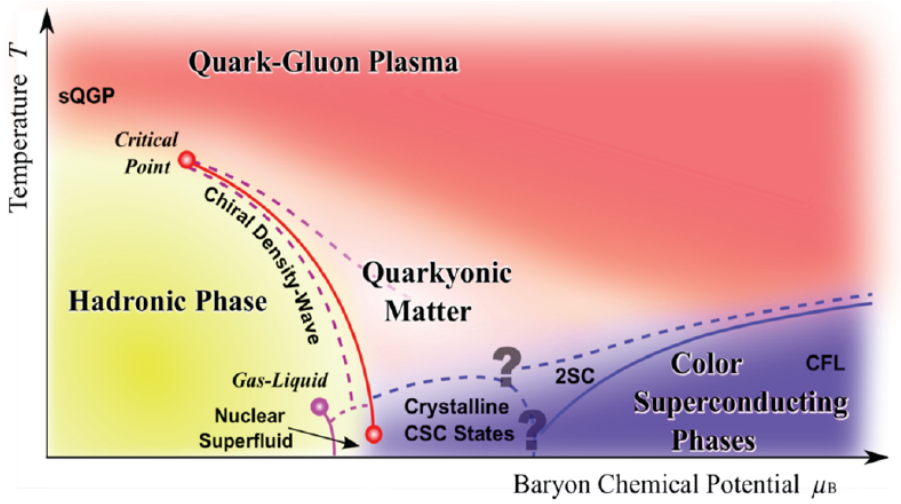

Figure 2.1: Schematic sketch of the Quantum Chromo-Dynamics phase diagram, describing the phase states of strongly interacting matter at different temperatures T and baryon chemical potentials μ_B [17].

as A Large Ion Collider Experiment (ALICE) at CERN, analyzing collisions of protons or heavy lead ions at very low net-baryon densities, which are accelerated by the Large Hadron Collider (LHC) [25]. For higher densities and moderate temperatures, however, the QCD phase diagram assumes a critical point with a first-order phase transition to the quarkyonic phase. Other experiments, like the STAR collaboration at RHIC or the heavy-ion collider NICA at JINR, try to analyze nucleon collisions in order to find out about the QCD critical point or the coexistence phase of nuclear matter [2, 8].

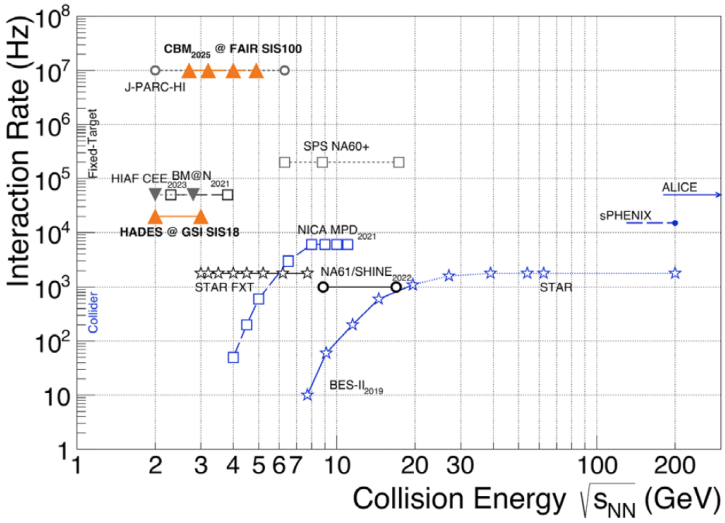

Figure 2.2: Interaction rates and collision energy $\sqrt{s_{NN}}$ of different collider experiments [21].

Due to limiting factors, such as luminosity or the detectors, though, these experiments have difficulties in providing enough statistics of rare probe measurements. This issue is approached by the Compressed Baryonic Matter (CBM) experiment at the Facility for Antiproton and Ion Research (FAIR) in Darmstadt. As shown in Figure 2.2, CBM is planned to be able to reach an interaction rate of 10 MHz. Considering the high baryon-chemical potential expected during the collisions at SIS100, the CBM experiment will provide sufficient results to investigate the QCD at high net baryon densities and the possible first-order phase transition. SIS100 and CBM are currently under construction and are planned to be finished and commissioned in 2028. CBM will operate as a fixed-target experiment to examine the high net baryon density collisions.

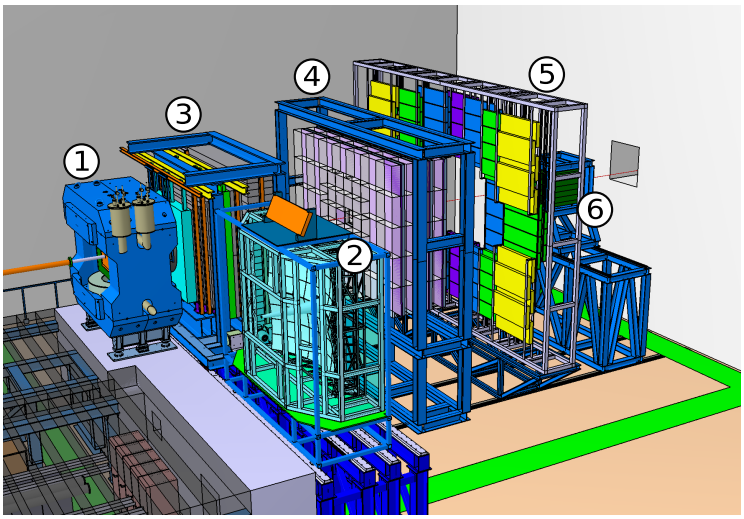

Figure 2.3: Computer-Aided Design (CAD) illustration of the CBM experiment at FAIR with all enumerated detectors. Modified from original [5].

With its rigidity of $R = 100\,\mathrm{Tm}$ the SIS100 is able to provide beams from protons to heavy nuclei up to uranium, so that proton-nucleus and nucleus-nucleus collisions with different beam energies can be performed. For instance, Au-Au collisions can reach a center-of-mass energy of $\sqrt{s_{NN}} = 4.9\,\mathrm{GeV}$ [21], while proton-nucleus collisions can reach even higher center-of-mass energies. The detection of events after the collision is done by a series of detectors, which are shown in Figure 2.3, each focusing on different aspects of the collision.

1 Dipole Magnet The superconducting dipole magnet provides a vertical magnetic field with a magnitude of 1 T, which deflects incoming particles in an opening angle of ±25 ° vertically and ±30 ° horizontally [6].

In 1: Target As CBM is a fixed-target experiment, the target is a stationary foil, placed within the dipole magnet.

In 1: Micro-Vertex Detector (MVD) The MVD is the first detector downstream of the target and is responsible for tracking low momentum particles with high-precision in direct proximity of the target. It uses four layers of monolithic active pixel sensors. The MVD will only be placed during runs with moderate interaction rates, due to its rate capabilities.

In 1: Silicon Tracking System (STS) Right after the MVD, the STS is used to identify charge and momentum of the particles that are created after the beam-target interaction, by tracking the particle trajectories. This system consists of eight measuring units, which use double-sided silicon microstrip sensors for detection. It matches the azimuthal acceptance of the dipole magnet except for the centered beam pipe, which consumes ±2.5 °. Together with the magnetic field, a momentum resolution of $\Delta p/p < 2\,\%$ can be achieved [6].

2 Ring Imaging Cherenkov Detector (RICH) With CO_2 as a radiator, spherical mirrors and multianode photomultipliers, the RICH System identifies electrons with momenta under 8 GeV/c by detecting their Cherenkov rays and therefore suppresses pion background. It is located behind the STS downstream of the target when the experiment runs in electron setup.

3 Muon Chamber System (MUCH) The muon detection system consists of six layers of hadron absorbers. Each layer has additional iron plates and gas chambers, which track passing particles and determine muons based on their momenta. This system is designed as compact as possible to prevent further meson decays into muons. MUCH replaces the RICH system when the experiment runs in muon setup.

4 Transition Radiation Detector (TRD) The TRD system contains four detector layers, of which each second layer is rotated by 90 °. Using Multiwire Proportional Chambers (MWPCs) and the transition radiation of the particles, incoming positrons and electrons with $p > 1\,\mathrm{GeV/c}$ can be identified [5]. The system is located either after the RICH or after the MUCH system.

5 Time-of-Flight System (TOF) The TOF system is placed right behind the TRD and consists of an array of multi-gap resistive plate chambers, that identify hadrons based on their time-of-flight to the TOF-wall.

6 Fragment Spectator Detector (FSD) The last detector downstream of the target is the FSD, which is responsible for examining the centrality of the beam-target interaction by measuring non-interacting particles from the beam.

Since this thesis focuses on the determination of the electrode wire tension inside the TRD, the following chapters will give more detailed descriptions on the TRD principles, the importance of the wire tension as well as its determination process by the WTTD.

Chapter 3

The transition radiation detector

The working principle of the TRD is based on that of gaseous ionization detectors. A particle passes through the entrance window of the detector and deposits parts of its kinetic energy to the gas atoms. For charged particles with a specific mass and certain momenta, this deposition of energy in a medium can be calculated by the Bethe-Bloch formula. For photons, however, the energy loss is characterized by the interactions with other particles of the medium, e.g. the photoelectric effect, Compton scattering and pair production [13]. Thus, the gas atoms are ionized and electron-ion pairs are created, which drift to the electrodes due to an electric field that is applied through a voltage supply. When these electron-ion pairs reach the electrodes, a current can be measured that indicates the particle that passed through the detector. Based on this mechanism, there are three different types of gaseous ionization detectors.

Ioniziation Chambers operate at low electric potentials, causing the electron-ion pairs to not trigger avalanches. Only the primary ions and electrons drift to the electrodes, so that there is no gas amplification of the initial charge. That results in a small measured current without any dead times, in which the chamber cannot measure other incoming particles. Another form of these detectors is the **Proportional counter**. These detectors operate at higher electric field strengths, that lead to gas amplifications where the electron-ion pairs trigger an avalanche. In comparison to the ionization chambers, the output current is not continuous but a pulse that is proportional to the deposited energy of the detected particle. The last type is the **Geiger-Müller Tube**, which operates at even higher voltages, so that not only one but multiple avalanches are generated by the electron-ion pairs and additional UV photons. This results in a gas amplification that is independent of the deposited energy of the particle and always leads to high current pulses and higher dead times.

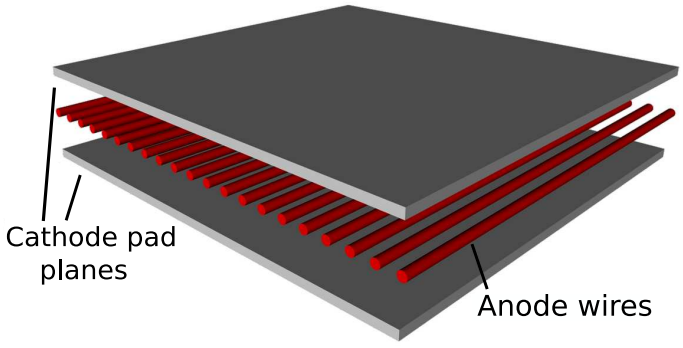

Figure 3.1: Schematic view of a Multi Wire Proportional Chamber with anode wire and cathode pad plane. Slightly modified from original [12].

The Read Out Chambers (ROC) used within the TRD are based on Multi Wire Proportional Chambers (MWPC), which are a type of proportional counter. The advantage of proportional counters, in terms of fulfilling the tasks of the TRD, is that, because the gas amplification only depends on the initial charge, different energy losses of incoming particles also cause different current outputs and thus can be identified. This is important for distinguishing between pions and electrons or positrons in the TRD measurements. The multiwire chamber form can be achieved by simply stringing multiple proportional counters next to each other. The outcome is a chamber with an anode wire plane in the middle and two cathode planes enclosing the wires, as shown in Figure 3.1. With these MWPCs, a one-dimensional spatial resolution is provided and with an additional MWPC rotated by 90 ° behind the first one, a two-dimensional resolution can be achieved.

3.1 Multi Wire Proportional Chamber in the CBM TRD

The exact design of the MWPCs used in the TRD is pictured in Figure 3.3. As can be seen, the first element of the detector is a 30 cm thick radiator in front of the entrance window. Its purpose is to provide multiple media transitions so that traversing electrons and positrons emit transition radiation (TR). Transition radiation is a phenomenon that occurs when charged particles travel through a boundary between two media with different dielectric constants. One way of explaining the creation of TR photons is via the difference between the inhomogeneous Maxwell equations in the two media that equals the TR photon. This means that because the electric field of the particle is different within the two media, it needs to emit this difference as a TR photon. The emission of these photons is directed alongside the traveling direction of the charged particle, distributed in a cone with the angle θ and peaking at the angle $\theta_{\max} \approx 1/\gamma$ [13]. For one interface crossover, the entire intensity of the radiated energy increases linearly with the Lorentz factor:

$$\gamma = \frac{E}{m} \tag{3.1}$$

with the energy E and the mass m of the charged particle. This enables the TRD to distinguish between pions and electrons. The mass of pions[1] is about 273 times higher than that of electrons[2], thus their Lorentz factor is lower and they emit almost no TR photons when passing through the radiator. However, the entire intensity of the radiated photons is very low, due to its dependency on the fine structure constant $\alpha = \frac{1}{137}$. Accordingly, even electrons produce insufficient quantities of TR photons when traversing only a single interface between two media. A radiator which contains multiple media interfaces and causes the TR photons to interfere constructively solves this problem. For the CBM-TRD, polyethylene foam foils are used for this purpose.

For high relativistic particles with $\gamma > 10^4$ the radiated energies reach into the X-ray domain [13]. For this reason, the chamber between the entrance window and the cathode pad plane is filled with 85 % xenon and 15 % carbon dioxide. The xenon has a high gas amplification in comparison to other noble gases and also provides a high absorption cross section for photons in the X-ray domain. As depicted in Figure 3.2, the absorption length for typical TR photons with energies within the X-ray domain is in most cases lower in xenon than in argon or krypton. Especially for typical TR photons with energies below 10 keV, the absorption length is less than 10 mm. With this, the chamber thickness as well as the signal collection time can be reduced, which is important for measurement precision at such high interaction rates.

[1] Charged pions: $m_{\pi^-} = 139.6 \frac{\text{MeV}}{c^2}$ and $\gamma_{\pi^-} \approx 7$ with $E_{\pi^-} = 1\,\text{GeV}$ [24].
[2] Electrons: $m_{e^-} = 511 \frac{\text{keV}}{c^2}$ and $\gamma_{e^-} \approx 1956$ with $E_{e^-} = 1\,\text{GeV}$[24].

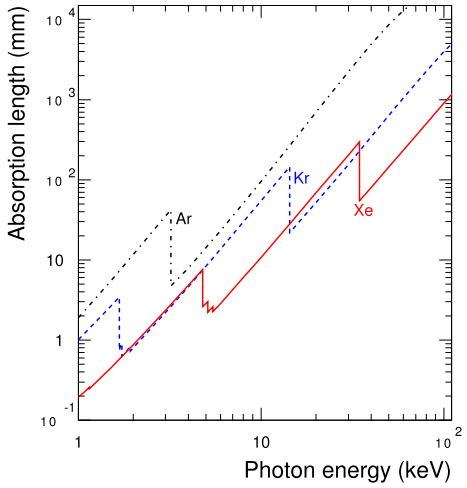

Figure 3.2: Absorption length for X-ray photons in argon, krypton and xenon [5].

The MWPC also contains a cathode wire plane, creating a drift region between itself and the entrance window with a distance of 5 mm. The reason for this additional drift region is to increase the probability of TR photons getting absorbed by the xenon atoms, by simply expanding the gas volume without enlarging the size of the amplification region, which would lead to an increased charge collected at the anode wires. The entrance window is supplied with a voltage of -500 V while the cathode wire plane is at ground potential. In a 3.5 mm distance to the cathode wire plane, the anode wire plane is located. Another 3.5 mm above the anode wires, the cathode pad plane completes the MWPC and forms the amplification region, together with the two wire planes. The wires in both wire planes are separated by 2.5 mm from the adjacent ones and furthermore, the anode wires are horizontally shifted to the middle of the gap between the cathode wires, as can be seen in Figure 3.3. To complete the amplification region, a voltage of 1850 V is applied to the anode wires, while the cathode pad plane is grounded. This arrangement of the wire planes was the best result of simulations in terms of the electric field, which is homogeneously shaped in the drift region and centered towards the anode wires in the amplification region.

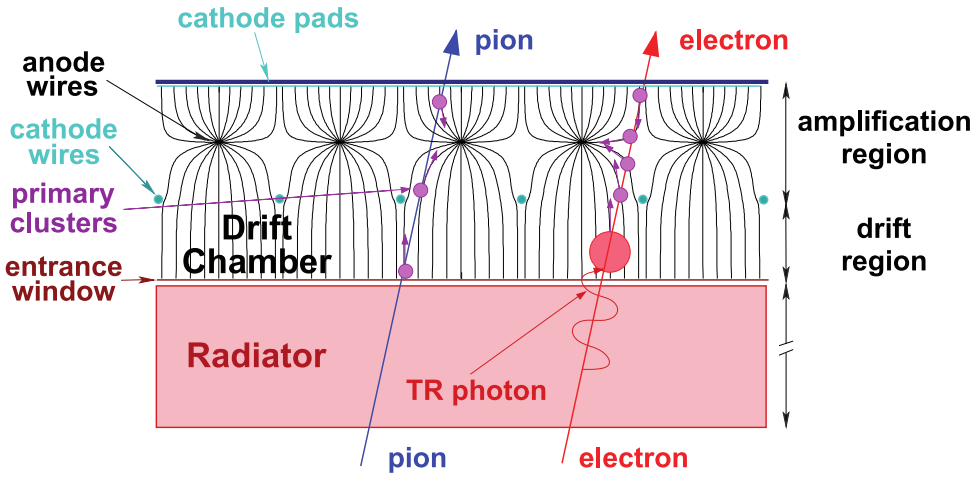

Figure 3.3: Schematic illustration of the MWPC used in the TRD, together with the Radiator in front of the entrance window [5].

As soon as the electrons and positrons enter the TRD MWPC, the electrons created by the interactions between TR photons and the initial electrons/positrons with the gas atoms are collected at the anode wires. Using the phenomenon of mirrored charges, this collected charge is induced to the cathode pad plane. To minimize the amount of readout electronics, only the signal induced on the pad planes is used.

As shown in Figure 3.4, the pad planes are divided into multiple rectangular pads with various sizes, to achieve a two-dimensional granular resolution. Their length, which is perpendicular to the wires, is always a multiple integer of the anode wire pitch of 2.5 mm, while their width, along the wires, is determined by the distance between the cathode pad plane and the anode wire grid. This structure of the MWPC intends to achieve a charge detection distribution of 80 % on the corresponding pad of a central hit and 10 % each on the adjacent pads. The charge distribution induced on the cathode pads is estimated by the Pad Response Function (PRF), which has the form of a Gaussian function. With all these aspects and a second TRD layer rotated by 90 ° behind the first, a two-dimensional spatial resolution below 300 μm to around 400 μm can be achieved [5].

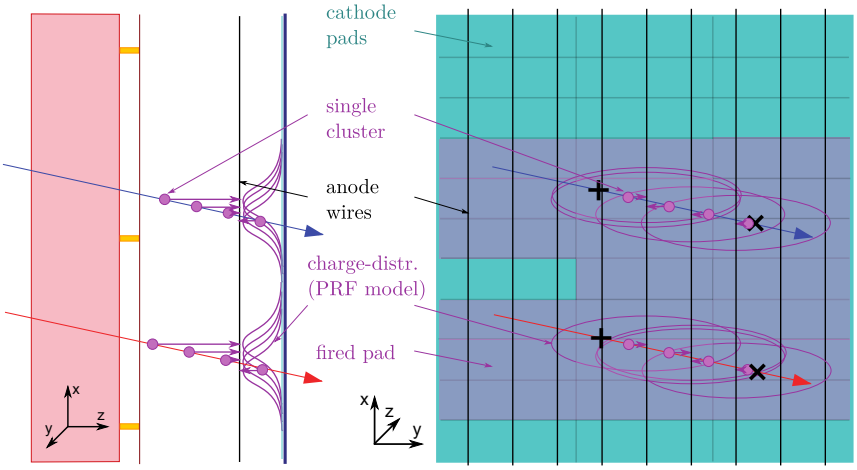

Figure 3.4: Schematic illustration of cathode pad plane and the PRF, that depicts the charge distribution of the charges, created by traversing charged particles [5].

3.2 Construction and production of the Read Out Chambers

The complete composition of the ROCs used in the CBM TRDs is depicted in Figure 3.5. First, there is the aluminium support frame on which the backside of the pad plane is glued. This backside consists of a carbon fiber plane together with a 23 mm thick honeycomb structured plane. To grant access to both the interior space and the pad planes, the backpanel provides feed-throughs for gas and high voltage. Furthermore, aluminium frame and backpanel also contribute to the mechanical stability and the compensation of the wire tension.

The interior space begins right after the cathode pad plane and contains the gas volume as well as the anode and cathode pad plane. These planes are separated from one another by distance ledges that have the required thickness to achieve the previously mentioned distances of 3.5 mm, 3.5 mm and 5 mm (see Section 3.1). A special winding machine winds the wire planes to both sides of a transfer frame, with the pitch of 2.5 mm. After fixating the wires with glue, the frame is divided in half so one winding process creates wire planes for two readout chambers. The transfer plane is then lowered to a distance ledge until the wires rest on top of it. After applying a thin film of glue onto the wire ledges, a second distance ledge is put on top of the film to keep the wires in position. After the glue hardens, the wires can be cut off the transfer frame and the process can be repeated for the second wire plane. Between the attaching of the wire planes, their tension should be checked with the WTTD to prevent the construction of malfunctioning ROCs due to incorrectly taut wires.

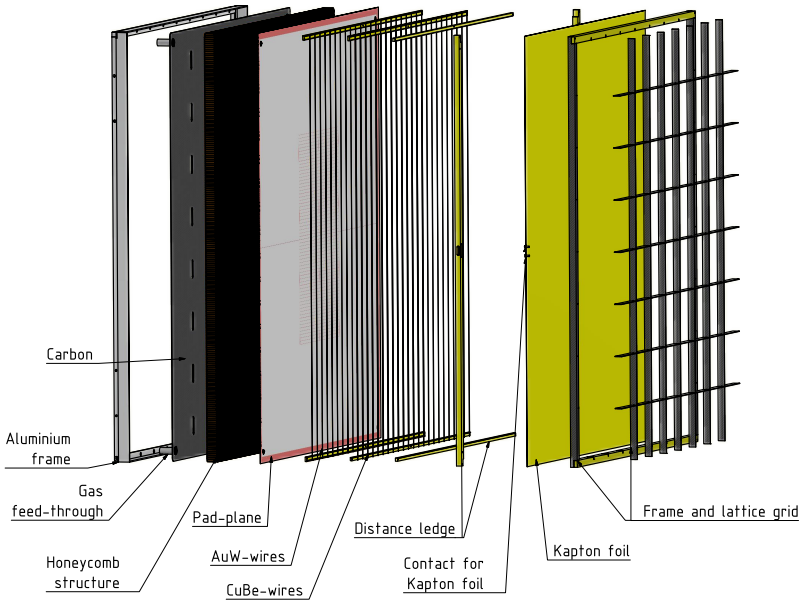

Figure 3.5: Exploded view of the computer generated design of the MWPC in the TRD [5].

After the anode and cathode planes are successfully winded and glued to the ledges, the entrance window can be attached to the distance ledge glued on the cathode wire plane. For that, a 25 μm thick Kapton foil with 0.05 μm aluminium on one side is used. It also has a contact on the side for electrical connection as the foil serves as an anode for the drift region. Because of the pressure in the gas volume, the foil is deflected and bulges to the outside of the detector which leads to gain variations. For this particular reason, a carbon support grid is added on top of the entrance window to ensure low bulging of the foil. This lattice grid marks the last element and completes the structure of the detector chambers.

3.3 Structure of TRD layers

The TRD layers used in the CBM experiment consist of four different modules of the already described MWPCs. As can be seen in Figure 3.6, the module types 5 and 7 occupy the two outer columns on each side, while type 1 and 3 fill up the center of one layer. There are only two different variations of the outer dimensions of the modules, but their arrangement of the pad numbers and sizes varies. The exact dimensions and numbers of the modules are listed in Table 3.1. The reason for this arrangement of the

Figure 3.6: Sketch of the module arrangement in one TRD layer [5].

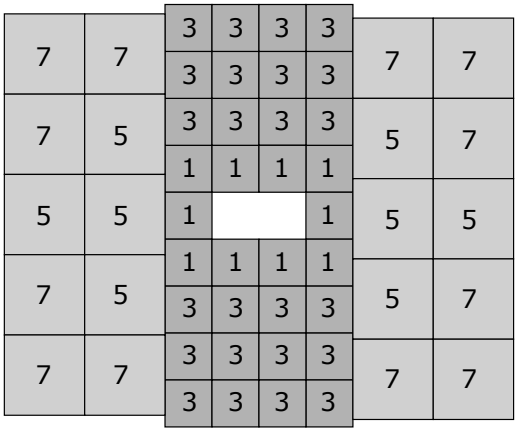

different modules deviates from the fact that the particle flux increases the closer to the center of one layer. Thus, the pad density for each module is adjusted to ensure low hit rates per readout pad. In general, the whole TRD system consists of four layers of which the modules are rotated by 90 ° per layer to achieve the previously mentioned two-dimensional spatial resolution. With a total number of 216 modules and 329 728 pads, the readout electronics include almost 33 000 readable channels.

Module type	1	3	5	7
Size	small		large	
Number per layer	10	24	8	12
Outer Area in cm	57 × 57		99 × 99	
Active Area in cm	54 × 54		96 × 96	
Pad rows × columns	32 × 80	8 × 80	24 × 144	8 × 144
Pad number	2560	640	3456	1152
Pad height × width in cm	1.75 × 0.68	6.75 × 0.68	4.00 × 0.67	12.00 × 0.67

Table 3.1: Summarized values of pad and module numbers and their dimensions in the different TRD modules [5].

3.4 Wire sag and determination of the wire tension

The goal of this section is to point out the importance of the mechanical wire tension regarding the sag that occurs on the anode and cathode wires. Additionally, the principle of the determination and how this process is automatized will be explained in the following.

3.4.1 Electrical field in the MWPCs

To achieve an equal gas amplification for the electron clusters over the entire area of the ROC, it is important that the electrical field also prevails equally arranged. That means that on the one hand, the electrical field in the drift region of the ROC is homogeneous and on the other hand, that the field within the amplification region is evenly shaped around each anode wire, as represented by the field lines in Figure 3.7.

The electrical field is generated by the wires with a radius r. For simplification, the wires can be treated as line charges in free space with the length L and the charge Q, so that the form of the field follows as [23]:

$$\vec{E}(r) = \frac{Q}{2\pi\epsilon_0 L\, r}\,\vec{e}_r \tag{3.2}$$

where ϵ_0 is the electric field constant. It can be seen that the electric field becomes stronger towards the center of the wire. A smaller radius of the wire therefore leads to a greater field strength in close proximity to it, which is why the anode wires have a radius of only $r_\mathrm{a} = 10\,\mu\mathrm{m}$. This thickness leads to a sufficient charge amplification in the ROCs while achieving the desired charge distribution on the cathode pads.

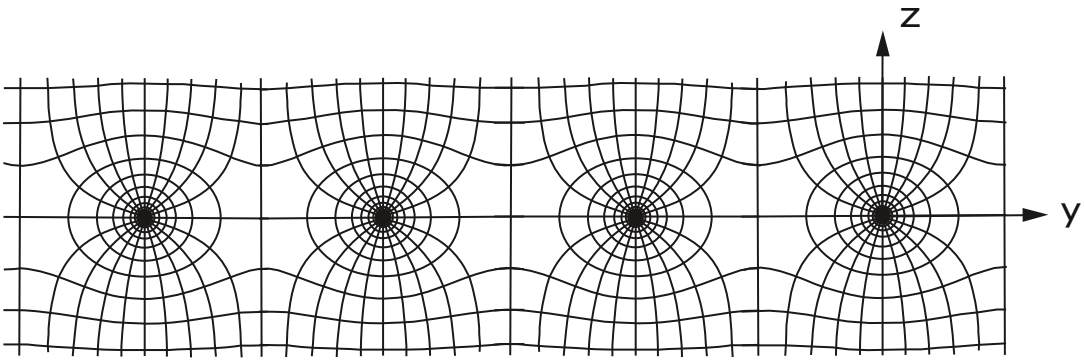

Figure 3.7: Skit of the electrical field lines in the amplification reigion. It transitions from a homogeneous field (top and bottom) to a radial symmetric field near the anode wires [13].

3.4.2 Wire sag – electrostatic and gravitational force

Because the wires generate the electrical field, they need to be equally placed. As mentioned previously, the wire pitch in both the anode and cathode wire planes is 2.5 mm. However, there are forces acting on the wires and creating a sag which leads to a displacement. A wire with length L that is stretched by the tension T at both ends sags due to the deflecting force F_d which in this case pulls the wire downwards. The magnitude of the sag $\Delta z(x)$ is described by the difference between the height of the attachment and the actual location of the wire in the z-direction. It depends on the x-location and has its maximum at the center x_c of the wire, which can be calculated by the formula:

$$\Delta z(x_\mathrm{c}) = \Delta z_\mathrm{max} = \frac{\alpha L^2}{8T} \tag{3.3}$$

with α being the proportional constant between $\mathrm{d}F_\mathrm{d}$ and the unit length $\mathrm{d}x$ [15]:

$$\mathrm{d}F_\mathrm{d} = \alpha\,\mathrm{d}x \tag{3.4}$$

As can be observed, $\Delta z(x)$ also depends on the tension with $\Delta z(x) \sim 1/T$, which shows that the magnitude of the sag decreases with rising tension.
The first contribution to the deflecting force F_d comes from the Coulomb force F_C, caused by the electric field 3.2 of the wires. Due to the electric potential between anode and cathode planes and the constant pitch in the wire planes, this force does not cause the wires to be displaced in the y-direction. Instead, they are pushed away in the z-direction, causing an alternating up and down formation, as shown in Figure 3.8 (left). The electric potential between the equally charged wires causes a repulsive deflection, while the potential between the wires and the oppositely charged pad planes causes an attractive deflection of the wire.

In addition to the electrostatic force, there is the own mass of the wire m that also contributes to the wire sag due to the gravitational force:

$$F_\mathrm{G} = m\,g = V\rho\,g = A\,L\,\rho\,g \tag{3.5}$$

With the gravitational constant g. The relations to the volume V, the density ρ and the cross section A of the wire will be useful in the upcoming chapter for determining the tension. Even so, the gravitational force does not have to contribute to the wire sag in any case. Due to the fact that every second detector layer is rotated by 90 ° and thus the wire planes run vertically in two layers, F_G has the opposite effect and weakens the emerging wire sag because it points in the direction of the wire tension instead of the Coulomb force.

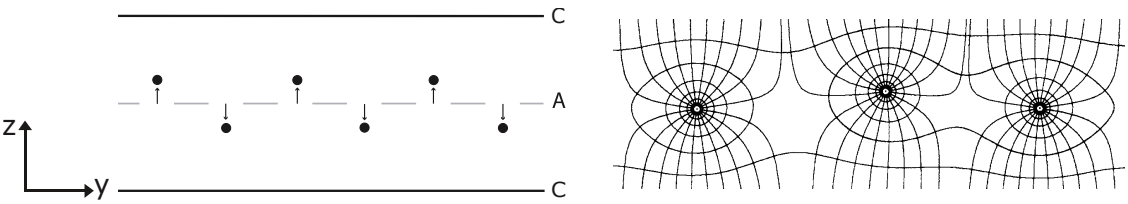

Figure 3.8: Alternating displacement of the anode wires (left) and the resulting distortion of the electric field (right) due to the deflection of the wires by the coulomb force within the MWPCs. [13, 10]

To prevent a too large sag, the Coulomb force and the gravitational force need to be extinguished by the vertical component of the tension. If that is not the case, then the wire sag causes the electric field to be unequally arranged around the wires, as shown in Figure 3.8 (right). This dislocation of the electric field leads to varying gas amplification and drift times of the charged particles at different locations in the ROC. An inconsistent signal readout and malfunctioning tracking abilities are therefore the consequences of such wire displacement.

As stated above, the wire sag gets smaller with higher tensions. But a simple, arbitrary increase of the wire tension is no expedient solution. Firstly, the chamber frame needs to be able to sustain the sum of all wire tensions. Otherwise, it will bend towards the center of the ROC, causing shorter and less tense wires. Secondly, having a wire under a tension T causes the stress [9]:

$$\sigma = \frac{T}{A} \tag{3.6}$$

to be applied to the wire. For rising stress under a certain stress limit σ_c, the wire deforms elastically, meaning that it shrinks back to its initial length after releasing the tension. But when surpassing the stress limit, the wire is inelastically deformed, causing a permanent deformation even after releasing the tension [9]. This stress limit, also called the yield point $R_e = \sigma_c$, is dependent on the material of the wire and should not be exceeded. Nonetheless, the applied stress should also be near this limit to ensure a sufficient amount of tension in order to keep the wire sag as low as possible.

Therefore, the anode wires consist of a tungsten rhenium alloy W + 3%Re that has a relatively high yield point of $R_e = 1639\,{}^{\mathrm{N}}/_{\mathrm{mm}^2}$. They are planned to be attached to the chamber frame with a tension of $T_a = 0.5\,\mathrm{N}$ which is equivalent to a stress of $\sigma = 1575\,{}^{\mathrm{N}}/_{\mathrm{mm}^2}$. Besides the high yield point, this alloy also exhibits good conductivity and is coated with gold to achieve a smooth surface for a uniform electric field. The cathode wires are made of a copper alloy with 2% beryllium, which is a lighter material in comparison to the rhenium alloy. They are also planned to be taut with a tension of $T_c = 1\,\mathrm{N}$ to compensate for the higher gravitational force on the cathodes due to their larger radius of $r_c = 37.5\,\mu\mathrm{m}$. Thicker cathode wires are desired because the electric field at their location needs to be as planar as possible and they can better balance the coulomb force between the anodes and the cathode pads. The exact characteristics of the anode and cathode wires are further summarized later in Table 3.2.

3.4.3 Determination of the wire tension

The next question that needs to be answered is how the tension of the wires can be estimated. Since they are highly sensitive, a mechanical measurement by stretching and physically touching the wires comes with the problem of plastic deformation, breakage and a damaged or polluted surface. Instead, the measurement should be done in an automatized process without any physical contact.

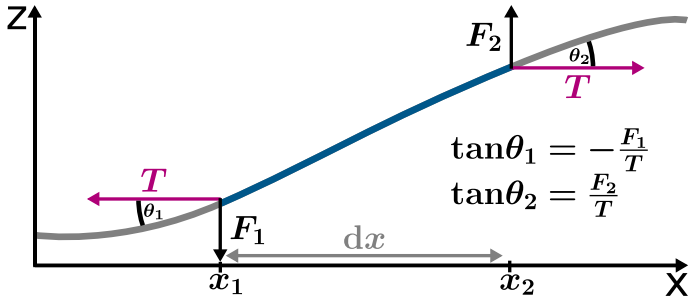

Figure 3.9: Increment of a stretched wire through which a wave is traveling. The transversal deflection can be described by the wire tension T and the vertical restoring forces F_1 and F_2. [15]

This can be achieved by deflecting the stretched wires by an air blast from a pressure surge air valve to trigger an oscillation. Simultaneously, an optical sensor scans this oscillation and sends its measured voltage to a computer where the values can be processed to reproduce the oscillation frequency. Shortly after the wires are deflected by the air blast, they start oscillating with their own fundamental frequency f_0. By measuring this frequency, the wire tension can be calculated, as will be derived in the following.

To establish the relation between the frequency and the tension, a transversal wave traversing through a plucked wire, taut with the tension T, is considered as in [15, 26]. As shown in Figure 3.9, a small increment of the wire with a mass of:

$$\mathrm{d}m = \mu\,\mathrm{d}x \quad \text{with} \quad \mu = \frac{m}{L} \tag{3.7}$$

can be regarded where μ is the linear density defined as the mass m per length L of the wire. As the wave runs through this increment in positive x-direction, the vertical restoring forces F_1 and F_2 cause the wire increment to move alternately in z-direction. The net force that acts on the increment is the sum of all forces, but since the wire tension is considered to be equal on both sides and remains constant in any position at any time, only F_1 and F_2 contribute to the net force:

$$F_{\text{net}} = F_1 + F_2. \tag{3.8}$$

The oscillating increment opens up the angles θ_1 and θ_2, which form triangles together with the tension on both ends of the increment, the respective restoring forces and the wire itself running diagonally, as illustrated in Figure 3.9. Therefore, the geometrical relations $\tan\theta_1 = -F_1/T$ and $\tan\theta_2 = F_2/T$ hold and since tan describes the slope of a function at a point, the fractions of the restoring forces and the wire tension can be written as the partial derivative of z with respect to x at points x_1 and x_2:

$$-\frac{F_1}{T} = \left(\frac{\partial y}{\partial x}\right)_{x_1} \quad \text{and} \quad \frac{F_2}{T} = \left(\frac{\partial y}{\partial x}\right)_{x_2}. \tag{3.9}$$

Inserting this into the net force 3.8 leads to:

$$F_{\text{net}} = T\left[\left(\frac{\partial y}{\partial x}\right)_{x_2} - \left(\frac{\partial y}{\partial x}\right)_{x_1}\right]. \tag{3.10}$$

Using Newton's second law, the net force can be replaced by the incremental mass and the acceleration a. Rewriting $\mathrm{d}m$ regarding Equation 3.7 and a as the second time derivative of y leads to:

$$F_{\text{net}} = \mu\,\mathrm{d}x\frac{\partial^2 y}{\partial t^2} = T\left[\left(\frac{\partial y}{\partial x}\right)_{x_2} - \left(\frac{\partial y}{\partial x}\right)_{x_1}\right]. \tag{3.11}$$

Dividing this by $T\mathrm{d}x$ and considering the limit of $\mathrm{d}x$ approaching zero yields:

$$\lim_{\mathrm{d}x\to 0} \frac{\left[\left(\frac{\partial y}{\partial x}\right)_{x_2} - \left(\frac{\partial y}{\partial x}\right)_{x_1}\right]}{\mathrm{d}x} = \frac{\partial^2 y}{\partial x^2} = \frac{\mu}{T}\frac{\partial^2 y}{\partial t^2}. \tag{3.12}$$

According to the one-dimensional linear wave equation [26]:

$$\frac{\partial^2 y(x,t)}{\partial x^2} = \frac{1}{v^2}\frac{\partial^2 y(x,t)}{\partial t^2} \tag{3.13}$$

one gets a relation between the wire tension and the speed v of the wave:

$$\frac{1}{v^2} = \frac{\mu}{T} \quad \Longleftrightarrow \quad v = \sqrt{\frac{T}{\mu}}. \tag{3.14}$$

Putting this into Equation 3.7 and replacing m with the density ρ and cross section A of the wire according to Relation 3.5 gives:

$$v = \sqrt{\frac{T}{\rho\, A}}. \tag{3.15}$$

Besides this equation, the speed of a wave can also be calculated via the condition that the length of the wire must be an integer multiple n of half the wavelength λ of the wave:

$$L = n\,\frac{\lambda}{2} \quad \text{and with } \lambda = \frac{v}{f}: \quad v = \frac{2Lf}{n} \quad \text{with} \quad n = 1, 2, \dots, \tag{3.16}$$

otherwise destructive interference causes the wave to cancel itself. Now, both Relations 3.15 and 3.16 can be equated and then rearranged to calculate the wire tension:

$$T = \frac{4}{n^2} L^2 f^2 \rho A. \tag{3.17}$$

Since the wire oscillates with its fundamental frequency f_0, it means that $n = 1$. Additionally, the cross section can be replaced with $A = \pi r^2$ so that a final formula can be obtained:

$$T = 4\pi\rho L^2 {f_0}^2 r^2 \tag{3.18}$$

Evidently, the tension of the taut wires depends on their length, radius, density of the material and their fundamental frequency. If the frequency can be reproduced from the voltage samples of the sensor, the tension can be calculated and compared to the desired wire tensions of $T_\mathrm{a} = 0.5\,\mathrm{N}$ and $T_\mathrm{c} = 1\,\mathrm{N}$. When rearranging this equation in order to get the fundamental frequency, it can be determined by plugging in the wire properties listed in Table 3.2. These frequencies are expected to be extracted from measuring the wire oscillation and were calculated in Table 3.2 as well.

	Anodes in 1 & 3	Anodes in 5 & 7	Cathodes in 1 & 3	Cathodes in 5 & 7
Material	W + 3 % Re (Au-plated)		Cu + 2 % Be	
Wire number per plane	216	384	216	384
Density ρ in g/cm^3	19.3		8.15	
Radius r in μm	10		37.5	
Cross section A in mm^2	$3.142 \cdot 10^{-4}$		$4.418 \cdot 10^{-3}$	
Tension T in N	0.5		1	
Length L in cm	54	96	54	96
Frequency f_0 in Hz	266	150	154	87

Table 3.2: Values of the characteristics of the anode and cathode wires in the different TRD module types. [5]

3.4.4 Fourier analysis

After the wire oscillation gets measured by the sensor, the resulting voltage values need to be processed by a certain method in order to extract the frequency. One possible way is using curve fitting methods that numerically estimate the best parameters of a function to a data set. However, these methods are highly sensitive to noise and other disturbing signals. Another way of reproducing the fundamental frequency is to calculate the Fourier transformation, which provides sufficient noise reduction and is therefore the chosen method in this thesis.

Since the sensor output consists of discrete voltage samples, a Discrete Fourier Transformation (DFT) is used. The DFT takes a given sequence x_n containing a finite number of N samples and estimates the corresponding Fourier transformation X_k via the sum [27]:

$$X_k = \sum_{n=0}^{N-1} e^{-2\pi i \frac{kn}{N}} x_n \tag{3.19}$$

with the imaginary unit i and the index k that marks each frequency term and ranges from 0 to $N-1$. The first term $k = 0$, for example, is calculated by the sum:

$$X_0 = \sum_{n=0}^{N-1} x_n \tag{3.20}$$

and corresponds to the zero frequency f_0. For N even, $k = 1 \dots N/2 - 1$ represent the positive and $k = N/2 \dots N-1$ the negative frequency terms. For N odd, $k = 1 \dots (N-1)/2$ and $k = (N+1)/2 \dots N-1$ instead represent the positive and negative frequency terms. These values of X_k are mapped to the corresponding frequencies f_k that range from $-f_{\mathrm{Nyq}}$ to f_{Nyq}. This limit is called the Nyquist frequency and is determined by the sampling frequency f_{S}:

$$f_{\mathrm{Nyq}} = \frac{f_{\mathrm{S}}}{2} = \frac{1}{2\,\Delta t_{\mathrm{S}}} \tag{3.21}$$

with Δt_{S} being the time interval between each sample. Using f_{Nyq} as the limit derives from the Nyquist-Shannon sampling theorem, which states that a signal can only be

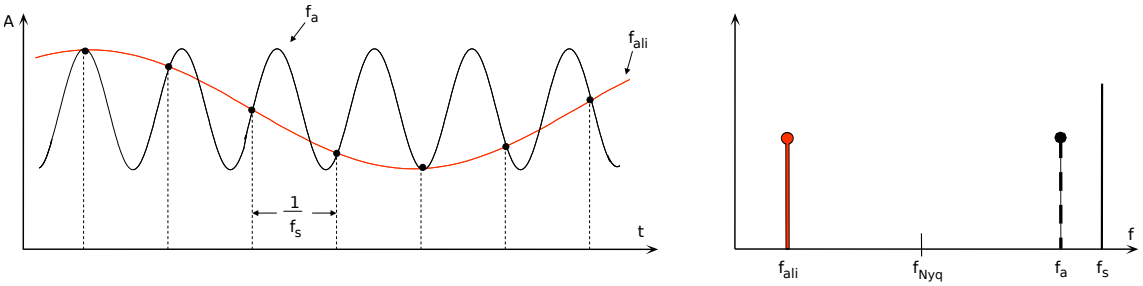

Figure 3.10: Example of a signal with frequency f_a that gets sampled by just a slightly higher frequency f_S so that the Nyquist-Shannon criterion is not fulfilled. On the left, the incorrectly reconstructed alias with frequency f_{ali} is shown in the time domain while on the right, its peak is given below the Nyquist frequency in the frequency domain. [28]

reconstructed if it is sampled at a sample rate that is at least twice the highest frequency component of the signal [7].
Since the DFT X_k is a sequence of length N, the frequency range f_k has to be of length N as well. This means the step width of the frequency spectrum depends solely on N, which in turn leads to a frequency resolution Δf_k that only depends on the duration of measurement t_S as long as f_S remains constant:

$$\Delta f_k = \frac{f_S}{N} \quad \text{with 3.21:} \quad \Delta f_k = \frac{1}{N\,\Delta t_S} = \frac{1}{t_S}. \tag{3.22}$$

With all this, the signal can be processed efficiently and the fundamental frequency of the wire oscillation should stand out as the first and highest peak when plotting the magnitudes X_k against the frequencies f_k.

It is important to note that positive and negative frequency magnitudes only differ when a complex signal is sampled. If only real values are given, the negative frequency terms equal the positive ones but are simply mirrored onto $f_{N/2} \dots f_{N-1}$ or $f_{(N+1)/2} \dots f_{(N-1)}$. Since the sensor only provides real voltage values, the positive frequency terms are mirrored and it is therefore legitimate to only consider them. Additionally, the power spectrum of X_k can be calculated to only include the non-imaginary terms by multiplying X_k with its complex conjugate:

$$P(X_k) = \frac{{X_k}^* \cdot X_k}{N^2}. \tag{3.23}$$

Another aspect which has to be considered when doing the Fourier analysis of the signal is aliasing. This phenomenon appears when a frequency component of the original signal exceeds f_{Nyq} and is thus interpreted as a frequency below the Nyquist frequency. This leads to a false reconstruction of the signal frequency, as shown in Figure 3.10.

In the frequency spectrum, the first alias f_{ali} is found at:

$$f_{ali} = \pm\,(f_{Nyq} - |f_{original} - f_{Nyq}|) \tag{3.24}$$

and appears periodically with a distance of f_{Nyq} [27]. To prevent aliasing, f_S should be chosen high enough, especially since the fundamental frequencies of the wires are known. Besides, a low-pass filter can be applied to the data before calculating the DFT.

To ensure a low runtime of calculation, an algorithm called the Fast Fourier Transformation (FFT) is applied. Since the DFT in 3.19 requires N multiplications for N entries, the runtime scales with N^2, which makes it increase rapidly for larger data sets. On the contrary, the FFT has only a runtime of $O(N \log_2 N)$ because it uses a divide and conquer process to split the original calculation for the DFT into multiple, independent subcalculations that can be solved quicker. When recombining the solutions of these subproblems, the original problem can be solved.

Chapter 4

Setup and operation of the WTTD

As explained in the previous chapter, the wire tension will mainly be measured during the assembly process of the TRD ROCs to ensure the wires are wound onto the frames with the correct tension. In Figure 4.1, a schematic view can be seen that shows the design of the WTTD for measuring the wire tension in an open chamber. The frames together with the wire planes are put in the center underneath the linear drive. The sensor unit together with a valve which can be moved perpendicular to the direction of the wires is mounted laterally to the linear drive. A more detailed explanation of all the components, the working principle and the data transfer of the WTTD will be given in the upcoming chapters.

4.1 Components and their functioning

The current setup of the WTTD is shown in Figure 4.2. This device is still under development and is hence still missing some components, such as the housing of the motor and sensor elements, the cable carrier, etc. Furthermore, the preamplifier and the low-pass filter are planned to be brought together on a circuit board for the final setup. Nevertheless, all measurements and required component functionalities presented in this section can be conducted, given the current state of the WTTD. Their operation methods and their tasks will be described in detail in the following.

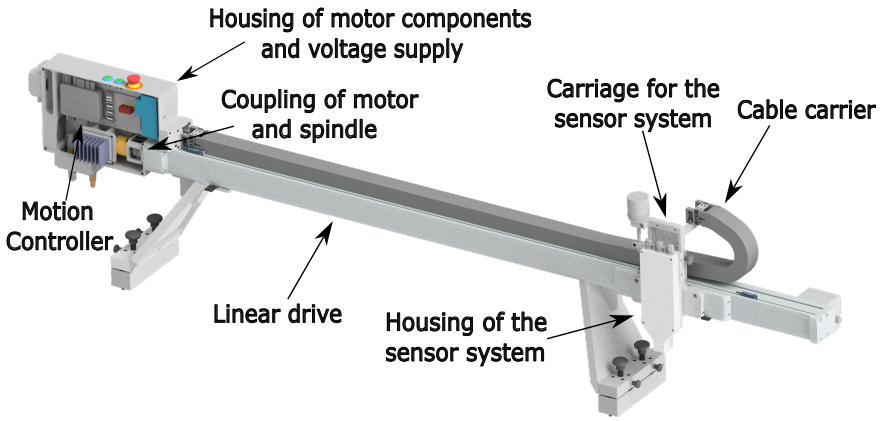

Figure 4.1: CAD sketch of the Wire Tension Test Device (WTTD).

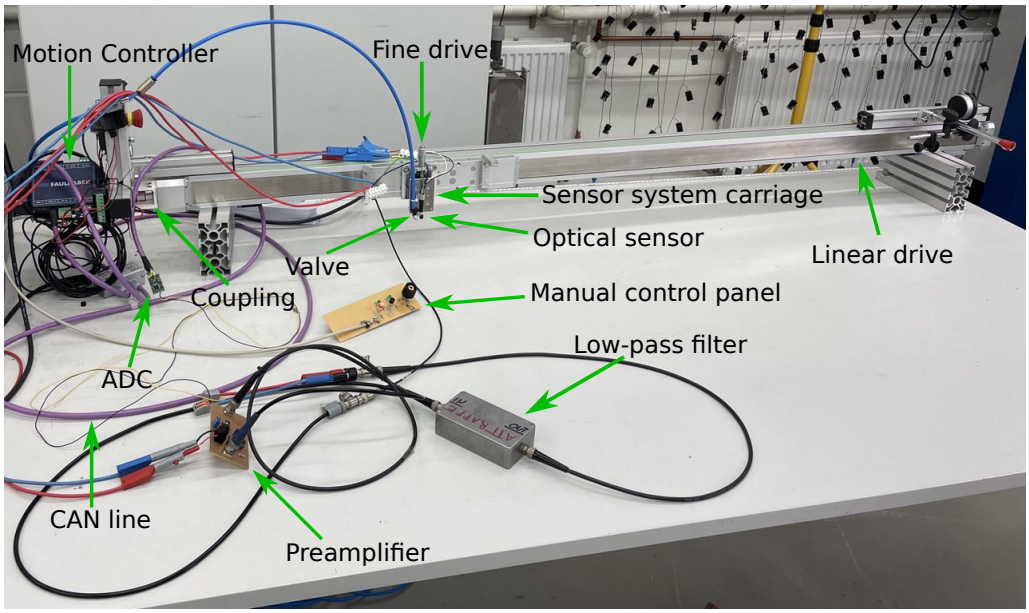

Figure 4.2: View of the current setup of the WTTD.

Linear drive The readout chambers will be placed underneath the 130 cm-long linear drive (*HIWIN HM060S005C1300S000C2NN*) which is positioned such that the sensor carriage runs through the center of the wire plane perpendicularly. The carriage is moved by a threaded spindle covered under a strip that has a feed constant of 5 mm and is rotated by the motor. The linear drive is currently placed on top of two aluminum mounts on each side.

Motion controller and motor The motion controller *Faulhaber MC 5005 S CO* is positioned directly in front of the left side of the linear drive. This device is connected to both the brushless direct current motor (*Faulhaber 4490H048BS*) which rotates the spindle and the magnetic encoder (*Faulhaber AEMT-12/16 L*) that breaks down each revolution of the motor into 4096 increments. This makes the Motion Controller the central unit for moving the sensor carriage as well as calculating the position of the carriage. An additional gear converts one revolution of the motor into a third revolution of the spindle. Therefore, the motor needs three revolutions in order to cover a distance of 5 mm which equals one revolution of the spindle. Furthermore, the Motion Controller comes with analogue and digital in- and outputs that are used for the manual control panel, the compressed air valve, the emergency stop button and the limit switches.

Sensor system The measuring unit for the wire oscillation begins with the reflective photosensor *ROHM Semiconductor RPR-220* which consists of an infrared-light emitting photodiode and a phototransistor that detects the reflected light and creates an output current, as shown in Figure 4.3. The reflection takes place on the surface of the wires and reaches its maximum at a focal length of 6 mm. For proper digitisation of the sensor output, a preamplifier is used to amplify the signal, before passing it through a low-pass filter to mitigate high frequency noise that appears when the sensor measures reflection (see Section 5.3). Finally, the processed signal reaches the Analogue to Digital Converter (ADC) *MicroControl sensor module µCAN.1.ai-SENSOR / voltage* that samples signals of $\pm 10\,\mathrm{V}$ with a frequency of $f_S = 1\,\mathrm{kHz}$. Given the expected fundamental frequencies from Table 3.2, this sampling rate should be sufficient to measure the oscillation of the wires properly.

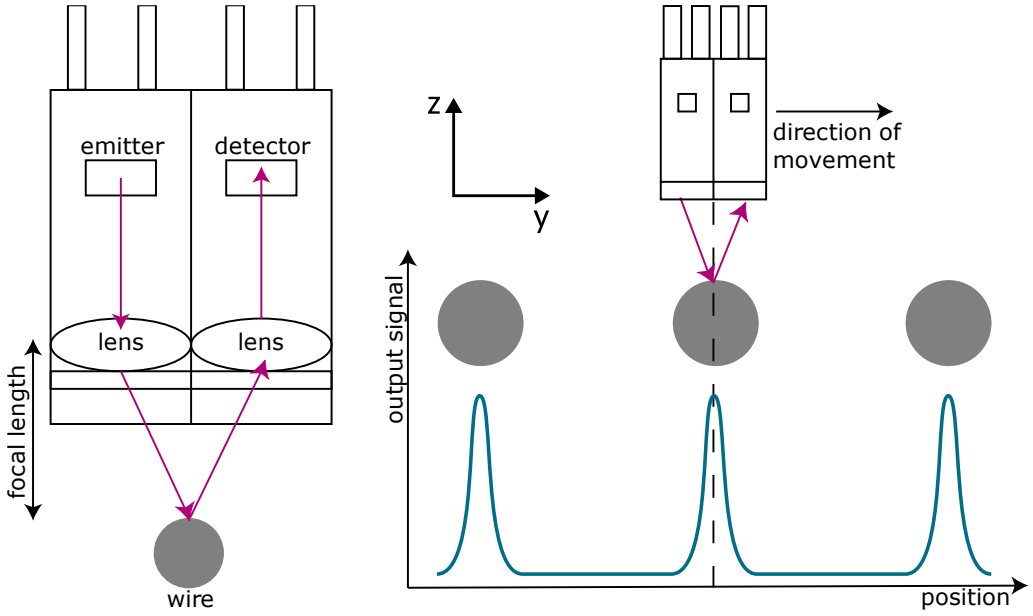

Figure 4.3: Illustration of the operation principle of the reflective photosensor RPR-220. The emitter is the photodiode which sends out infrared light that gets refracted by a lens. The wire is positioned in the focal point of the lens and reflects the light to the detector lens, where it gets refracted towards the phototransistor. The output signal in combination with the preamplifier is shown on the right side. [15]

Pressure surge air valve To trigger the wire oscillation, an air valve is used that emits an air blast towards the wire. It is mounted onto the carriage next to the reflective sensor. To ensure the wire oscillates in and out of the focal point in the direction of the wire plane, the air blast should also run in this direction. However, this cannot be completely achieved since the valve has to be on the same level as the wire plane. When moving across the wire plane, this causes physical contact and thus the risk of damaging or breaking the wires. Therefore, the valve is positioned such that on the one hand, it is still above the wire plane and on the other hand, the air is blasted laterally against the wires, so they are deflected mostly horizontally.

Connection and processing As depicted in figure 4.4, all electronic components are linked to two main cables (CAN-High and CAN-Low) of a Controller Area Network (CAN) bus that connects all devices to a computer via a USB-CAN adapter (*PEAK-System PCAN-USB*). A more in depth explanation about CAN will be given in the next section. All functionalities are implemented and executed in Python programs, which are stored on the computer.

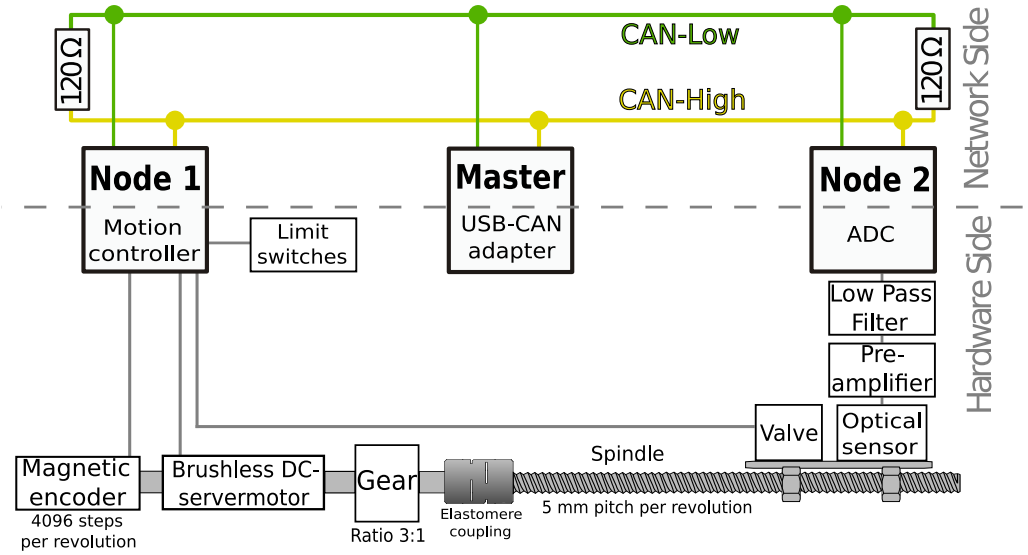

Figure 4.4: Schematic view of the connection lines of the WTTD. Modified from original. [15]

Manual control panel As already mentioned, a manual control panel is connected to the Motion Controller. It consists of two switches that move the carriage in each direction and a velocity wheel which sets the velocity of the movement. It is planned to use this panel to manually check the surface of the wires and the solder joints, with an additional microscope attached to the carriage.

Safety In order to avoid accidents from malfunctioning components, the WTTD has an emergency stop button that halts all devices. Furthermore, there are two limit switches at the ends of the linear drive as well as two moveable switches to adapt them to the different chamber sizes.

Housing To grant a safe storage of the Motion Controller and the sensor system, these components are planned to be mounted inside the respective housings (see Appendix B). For the sensor, the housing also provides further reduction of noise, created by the motor.

The wire tension measurement consists of a first run, in which the motor moves the sensor system along the wire plane while the output of the photosensor is constantly measured. As soon as the sensor measures reflection above a certain selectable threshold, the position is stored. After the position of all wires has been identified, the oscillation is measured in a second run. Here, the motor moves the carriage to each stored position, stops and activates the air valve, which hits the wire with its air blast. As the wire oscillates, the sensor measures the periodical reflection and outputs its voltage values. From these, the FFT is calculated, which shows the fundamental frequency of the wire.

To ensure that all components operate properly, they need to be supplied with the correct voltages. The Motion Controller, that also supplies the encoder, is fed with a voltage of 24 V. However, the motor must be provided with a separate voltage supply of 48 V. The sensor system on the other side needs to be powered by multiple voltage supplies of 12.34 V for the optical sensor, 10 V for the ADC and another 12 V for the preamplifier. To prevent reflection and ensure signal integrity, CAN-Low and CAN-High are terminated at each end of the bus with 120 Ω resistors, as can be seen in Figure 4.4. To cover the largest distance in the network of the WTTD setup, one resistor is located at the D-sub on the USB-CAN adapter while the other is soldered to the ADC. Looking at the setup in Figure 4.2, the CAN-High and CAN-Low cables are bundled inside the purple cable which

is referred to as the CAN line. It starts at the CAN adapter and runs into a CAN-Split 3000 pro cable splitter with four connections. From there, the CAN line splits into one line going to the Motion Controller, while another runs to the ADC. Besides CAN-High and CAN-Low, there are also two additional cables (GND and V_{cc}) running through the CAN line which are used for supplying the ADC with the required voltage. Via the fourth connection of the CAN splitter, they are connected to a power supply, providing this voltage of 10 V.

4.2 Controller Area Network

As mentioned before, the communication between the electronic components of the WTTD is realized via CAN. This system is based on CAN bus, a serial network architecture consisting of one main cable (the bus) to which all participating devices are connected. In this case, the main cable consists of the CAN-High and CAN-Low cables within the CAN line. Each device connected to the bus can transmit data to all other components and when receiving data, they can decide whether to accept and process it or ignore it. This results in a network in which all components can communicate efficiently without complex and expensive direct wiring. Together with a communication protocol such as CANopen, CAN bus can be fully centralized, as in this case, where all network diagnostics, functionalities and components (Nodes) are monitored and controlled by one device (Master). Furthermore, it is very resilient against electromagnetic interference in comparison to other network topologies.

CAN bus and CANopen can also be set in the context of the Open Systems Interconnection (OSI) model, which is a reference model dividing communication systems into seven layers, as shown in Figure 4.5. This model was developed by the International Organization for Standardization (ISO) and is recognized as the standard for describing and developing communication within technical systems [14]. In case of the OSI model, CAN bus covers the physical and data link layer, which are the lowest layers. In the physical layer, the mechanical connection between all network devices is established, while the data link layer secures data transmission by dividing the transfer of bits into frames. For covering the higher layers of the OSI model, CAN-based communication protocols are used with CAN bus. They primarily cover the application layer, but many of these, such as CANopen, also provide functionalities of other higher layers, e.g. the presentation, session, transport, or network layer. The exact bit sequence of a frame used in the data link layer of CAN bus as well as the main application elements of CANopen will be described below.

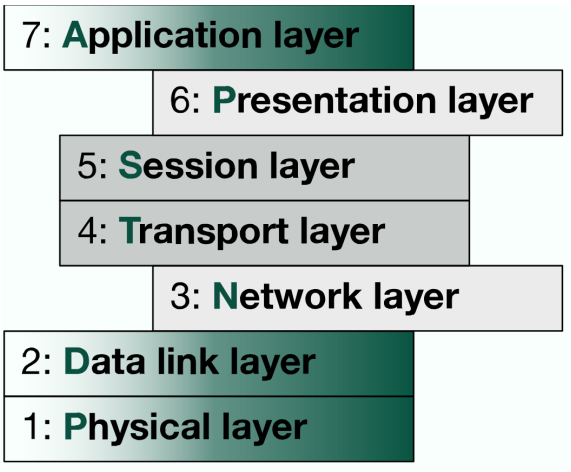

Figure 4.5: Schematic depiction of the OSI model with its different layers. The green colored layers are covered by CAN bus and CANopen. Elements of the other layers are often part of CAN-based applications, such as CANopen [4].

4.2.1 Data transmission on CAN bus

The data transfer on the bus is done via CAN messages. These messages are formatted by the CAN base frame that is depicted in Figure 4.6. The first bit of a CAN message is the starting frame, which contains either a dominant 0 or a recessive 1. The dominant and recessive bits deviate from the arbitration process that needs to be done to ensure interference-free communication when multiple nodes transmit data at the same time. This is because the data transmission on the CAN bus happens serially, which means only one message can be sent on the bus at a time. Therefore, when two nodes intend to send data at the same time, the arbitration process first checks the starting frame of the different messages. If one node sends a dominant 0 and the other a recessive 1, then the message with the dominant 0 is sent first while the node that sent the recessive 1 waits until no other dominant messages are on the bus [22]. Despite that, the arbitration of different CAN messages is continued by the next eleven-bit long Connection Object ID (COB-ID). With $2^{11} = 2048$ different addressable messages, messages with lower COB-ID are prioritized. It is therefore essential that each node and furthermore each object parameter of one node uses a unique COB-ID.

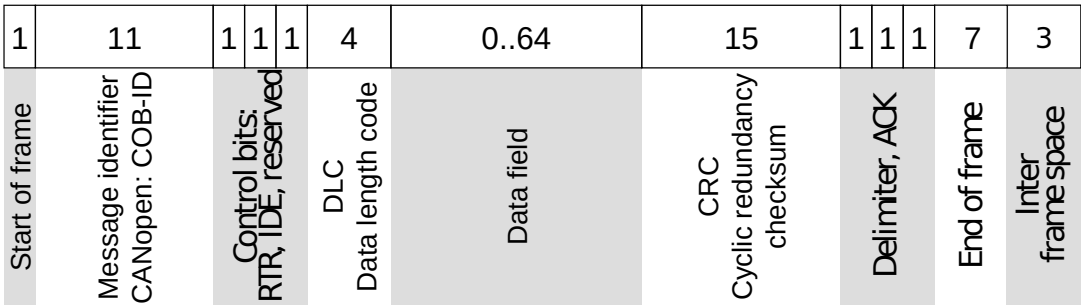

Figure 4.6: Schematic view of a CAN frame with the respective amount of bits for each frame section. [22]

After the arbitration is done, the Remote Transmission Request (RTR) and the Identifier Extension (IDE) follow, each occupying one bit. The RTR bit indicates whether the node sends data (dominant 0) or requests data from another node (recessive 1). The IDE bit on the other hand, shows whether the default length of 11-bit (dominant 0) or the extended length of 29-bit (recessive 1) is used for the COB-ID. After an additional reserved dominant bit, the Data Length Code (DLC) follows. Although it is 4 bits long, its values only range from 0 to 8 because it specifies the amount of bytes that are used in the data field of the CAN message. The data field comes right after the DLC and contains the content of the message, e.g. the settings of object parameters, measured values, etc. It can be up to 64 bits (8 bytes) long and is transferred in little endian byte order, meaning the least significant byte comes first, then the second least significant byte and so on. After that, the 15-bit long Cyclic Redundancy Check (CRC) comes to ensure data integrity. This is followed by the delimiter and the Acknowledgement (ACK) bit, together occupying 3 bits. Lastly, each CAN message ends with 7 recessive bits before the 3-bit long inter-frame space follows that always comes before a new message can be sent.

4.2.2 CANopen

After the data transfer is established by CAN bus, CANopen is used as the application. As already mentioned, it is a protocol that provides standardized and manufacturer-independent communication between all devices on a CAN bus. This is accomplished by the following main concepts of CANopen [19]:

Device profiles CANopen comes with a variety of communication profiles for different appliences and devices, which are made by CAN in Automation (CiA). For the setup associated with this thesis, the profiles CiA 301, 302 and 305 are used for the network, CiA 402 is used for the motion controller and CiA 404 for the ADC.

Communication models There are three types of models representing the communication in CANopen. The master-slave model describes the controlling of all nodes (slaves), which includes device state and configuration, by one node that acts as the master. In this case, the PC is the master while motion controller and ADC act as the two slaves.
Next is the client-server model, describing data requests from the client (PC) to the servers (other nodes). Data can be read and written which resembles up- and downloading data from servers by the client.
Lastly, the consumer-producer model depicts the broadcasting of data from a certain node (producer) that is in turn processed by another node (consumer). This can either happen with or without request from the consumer node.

Device states Each device on the bus can enter different states which determine its activity in terms of data transmission and processing. As explained above, the slave nodes do not change states by themselves but are controlled by the master. For example, when a device is connected to the bus for the first time it goes from "Initialising" to "Pre-operational" during bootup. In this state, it can process Service Data Objects (SDO), which will be explained later, from the master but can not broadcast data. Only after the master sets the nodes state to "Operational" it can transmit data on the bus. Analogously, the node can be changed back to "Pre-operational" to stop data transmission, or even to "Stopped" to deactivate it completely.

Object Dictionary (OD) and Electronic Datasheet (EDS) Every device on a CAN bus system must have an OD. This structure contains all parameters that describe the behaviour and the measurable quantities of the node. Each OD entry is assigned with an individual 16-bit index and 8-bit subindex and can be accessed by the master via SDOs to be configured. Some parameters are obligatory while others are completely optional, e.g. the filter of the ADC which can be turned on and off.
Furthermore, each node on the bus ideally comes with a EDS file that is typically provided by the manufacturer of the device. This file is a human readable form of the OD and contains a list of all its entries together with the related indices.

Communication protocol In CANopen, the actual communication protocol consists of several communication objects which are listed in Figure 4.7 with the respective COB-ID. Important to note is that the COB-ID in CANopen consists of firstly, the 4-bit long function code of the specific communication object and secondly, the 7-bit long node ID of the node which is communicated with. Together, they make up the 11-bit long COB-ID, as it was explained for the CAN frame in Figure 4.6. Furthermore, all bit-values in CANopen are represented in the hexadecimal system, which is why e.g. one byte from the data field only consists of two digits.

The first communication object is the **Network Management (NMT)** that is used for changing the device state of a node and can only be sent by the master. The NMT COB-ID has the node ID 0x0[1] in it which means that the message is processed by all nodes. The first data byte contains the state and the second byte the node ID of the device which should change into the desired state. Again, leaving the second data byte at 0x0 means all nodes on the bus change their respective state. Possible device states are 0x80 for "Pre-operational", disabling data broadcasting via Process Data Objects (PDO), 0x01 for

[1] 0x in front of any number indicates that it is a hexadecimal number.

"Operational", enabling all communication objects and 0x02 for "Stopped", disabling any objects except the NMT. Furthermore, nodes can also be reset with 0x81 for "Application reset" and 0x82 for "Communication reset".

The next communication element is the **Synchronization (Sync)** object. It is used to synchronize the measurement or actuation of several nodes and is sent out by the master. Sync messages can be sent periodically with an adjustable timer and also with or without a counter. Additionally, each node on the bus can be configured such that it either reacts to the sync or ignores it. E.g. for the wire localization measurement of the WTTD, the master frequently sends out sync messages which are replied to with two PDOs containing the measured voltage of the ADC and the position from the motion controller.

The purpose of the **Emergency (Emcy)** object is to monitor malfunctions in the network. It is sent out by a node as soon as it experiences any errors. There are several categories and types of errors that can occure which are specified in the data field of the emcy message. The exact emergency codes are typically defined by the manufacturer and can be looked up in the respective device manuals for CANopen.

The **Timestamp (Time)** object can be used to provide all network components with a current date and time information. The message is sent by the master and contains the time in milliseconds after midnight in the first 4 bytes as well as the number of days since January 1st, 1984, in the following 2 bytes.

The next communication object is called the **Service Data Object (SDO)** and it is the main tool for configuring the behaviour of the nodes. It is able to access and change the values of all parameters stored in the OD of a node. As for most communication objects listed in Figure 4.7, the COB-ID includes the targeted node. The first byte (command byte) contains the number of bytes that are either written to or read from the 16-bit index and 8-bit subindex of the parameter specified in the three following bytes. The last four date bytes of the SDO are filled with the exact values which the parameter should change into, in case of a write command. When the master successfully downloads data into an OD entry, the node responds with a Transmit SDO which carries the same four initial bytes as the SDO from the master, but has 0x0 in the rest of the data field. The same applies for uploading data, except that the last four bytes of the Transmit SDO contain the values which are read. In case of an unsuccessful down- or upload, e.g. because a parameter index was given that does not exist in the OD, the node responds with specifically defined SDO abort codes [20].

The **Process Data Object (PDO)** is a communication service for broadcasting data. As can be seen in Figure 4.7, there can be multiple PDOs, depending on the device, which must be assigned to a freely selectable OD entry of the node. This is called PDO mapping and needs to be done so the data field of the PDO can be fully used for actual data values. Hence, PDOs are able to transmit significantly more data than any other communication objects. The transmission of PDOs can be fully customized and ranges from event-driven, cyclical through synchronous. Event-driven transmission means the PDO is only sent once a change of the measured value occurs. Additionally, an event timer can be set that also triggers the transmission of the PDO after expiration, even when there is no change in measurement. In cyclic mode, only a timer triggers the transmission of the PDO while in synchronous mode, PDOs are sent after receiving a configurable number of sync messages which range from 1 to 240.

The last communication element CANopen provides is the **Heartbeat** message which is used for monitoring the state of a node. It contains the nodes device state in the first byte and can be configured to be sent periodically with a specific timer. The Heartbeat also occurs once whenever a node on the network is turned on.

Object	COB-ID (dec.)	COB-ID (hex)
Network Management	0	0x000
SYNC	128	0x080
EMERGENCY	129 - 255	0x081 - 0x0FF
PDO 1 (Transmit)	385 - 511	0x181 - 0x1FF
PDO 2 (Transmit)	641 - 767	0x281 - 0x2FF
SDO (Transmit)	1409 - 1535	0x581 - 0x5FF
SDO (Receive)	1537 - 1663	0x601 - 0x67F
Heartbeat / Boot-up	1793 - 1919	0x701 - 0x77F

Figure 4.7: Table of the communication objects provided by CANopen CiA 404. The COB-IDs are given for each possible node ID, ranging from 0x1 to 0x7F (1 to 127). Modified from original [20]

An example of a SDO request from the master is depicted in Figure 4.8. As can be seen, the COB-Id is 0x602, so in this case, the ADC with node number 0x2 is contacted. Via the OD index 0x1010, different parameter categories can be saved. With the subindex 0x01, all parameters of the ADC are saved. The command byte (CMD) contains 0x23, which indicates that four data bytes are written. More precisely, the four bytes contain the command word 'save' in ASCII (0x73617665). This request results in the following response SDO from the ADC, marked with the COB-ID 0x582. It contains the OD indices again, as well as the confirmation of the write command in the last four bytes of the data field with only zeros.

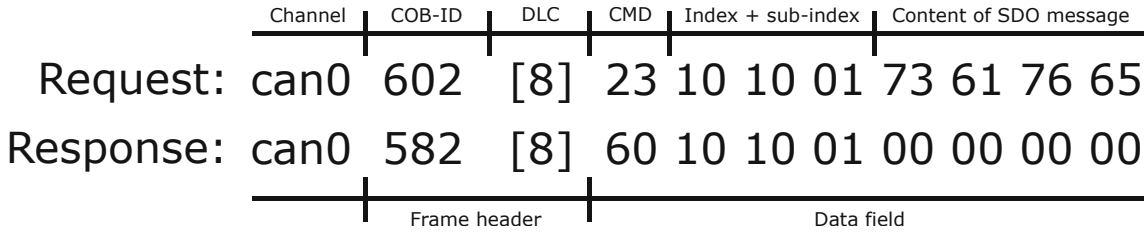

Figure 4.8: Example of a SDO save request from the master, answered by the confirmation SDO of the ADC.

Now that the network structure of the WTTD and the communication between all nodes via CAN bus and CANopen are clarified, the next step is to explain the control software for the WTTD. Hence, the following chapter focuses on the implementation as well as the calling of the functionalities of the motion controller and the ADC.

4.3 Software

The implementation of the device functions is done in Python via the CANopen package, which provides several commands and support for interacting with CANopen based networks. The main program, which boots up the whole network, runs all given procedures and finally deactivates the network, is shown in Listing 4.1.

First, four classes for the network, motor, ADC (here referred to as "Sensor") and test functions are implemented, before the network and both nodes are initialized by creating new objects for their class. For the network, the SocketCAN channel as well as the bitrate must be given, while the motor and ADC require the respective network and their individual node number. The bitrate determines how much data can be transmitted within a second. As for CANopen, typical values range from 10 kbit/s to 1 Mbit/s. The existence of lower bitrates is justified by the relation to the physical length of the bus. If the main cable exceeds certain lengths, the network cannot transmit data at the highest

bitrates and thus, lower ones must be chosen. In this case, simply the highest bitrate of 1 Mbit/s is selected, since the physical bus length of the WTTD is shorter than 25 m, which is the limit for this bitrate [20].

After that, the synchronization of the network with the given synchronization frequency $f_{\text{sync}} = 1/t_{\text{sync}}$ is started to request the position from the motor and the voltage from the ADC every t_{sync} seconds. It is important to add that the bitrate of the network, the synchronization frequency and the sampling frequency of the ADC are not the same and can be set individually. In the next step, the actual test functions and measuring procedures of the nodes follow, e.g. driving the sensor carriage to a certain position and activating the air valve. When this is done, the synchronization is stopped, alongside the motion controller and the ADC, before the network is disconnected.

```
from classes import Network, Motor, Sensor

Bitrate, sync_rate = 1e6, 1000 # in bits/s, Hz

# Connect to network and nodes by initializing the classes
network = Network(channel = "can0", bitrate = Bitrate )
motor = Motor(network, r"EDS_motor.eds", 1)
sensor = Sensor(network, r"EDS_sensor.eds", 2)

# Enable the operation of the devices on the network
motor.turn_on (); sensor.turn_on ()

# Synchronize the Motion Controller and the ADC
network.sync.start(1/sync_rate)

# ---------------------------------------
# All measure functionality follows here
# ---------------------------------------

# Stop the SYNC and finish the operation
network.sync.stop()
sensor.turn_off(); motor.turn_off()
network.disconnect()
```

Listing 4.1: Main program code for the operation of the WTTD written in Python.

The initialization of the WTTD includes configurations of the local network, the motor and the ADC. For the activation of the network, the driver for the USB-CAN adapter is checked and loaded into the Linux kernel when necessary. The bitrate of the network is checked to match between all participating nodes. In case of a non-matching bitrate, the Layer Setting Service (LSS) can be used to restart the network and change the bitrate of each node, in order to prevent miscommunication.
The initialization of the motion controller starts with a communication reset from the NMT, which triggers the bootup message. After that, the physical connection is checked and an error handler that outputs emergency messages is linked. Then, the mapping of the respective PDOs is done. Here, important parameters like position, speed and operation mode are added to PDOs. Additionally, the position PDO is set to synchronous transmission after every sync message. Finally, the state of the motor is changed to "Operational" and the motor can operate with certain control words, which are defined in the respective device profile CiA 402 of the motion controller.

Similarly, the activation of the ADC starts with a boot-up message as well. Due to the different device profile CiA 404 for the ADC, a reset is not needed during boot-up. Once this is done, the emergency callback is activated and PDO mapping is done. The only parameter that is needed from the ADC is the voltage output, which is also set to synchronous transmission. Lastly, the ADC is also set to "Operational" state by the NMT to start the operation.
A more detailed description of the initialization of all components is given in the thesis of J.Lämmel [15], as the preparation and implementation of the three classes for local network, motor and ADC as well as a variety of test functions were reached within his bachelor thesis project. Besides the initialization, there are also insights into the implemented operation of the motor and ADC given. In the course of this thesis project, additional test functions for the ADC were established such as `switch_to_continous_sampling` for changing its PDO transmission type or `measure_oscillation` which measures the wire oscillation via `candump`.

Chapter 5

Results

Before the results are presented in this section, it is important to mention that this thesis focuses on the sensor system of the WTTD because the ADC of the prior setup [15] had a maximum sampling rate of only 400 Hz. Considering the fundamental frequency of the anode wire in the small chamber modules (see Table 3.2), the ADC did not satisfy the requirements for sampling such frequencies correctly. Furthermore, the light reflection of the wire could not be registered in the optical sensor suggested at that time, making the sensoric components of the prior setup unsuitable for the wire tension measurements of the WTTD.

Despite this, all motor components were already investigated thoroughly by the prior bachelor project and proved themselves to be suitable for the WTTD. Different aspects such as position precision, repeatability and thermal expansion were examined and their results can be found in [15].

The evaluation of all data in this thesis was processed via Python. Data plots and function fits were created with the Matplotlib library. Parameter calculation was done with the Orthogonal Distance Regression (ODR) package provided by the Python-based open-source environment SciPy.

5.1 Synchronization speed of network

First, the time accuracy of the sync messages as well as the respective response latencies of the ADC and the motion controller were analyzed to compare them with those of the prior setup. There, 500 sync messages were sent with a frequency of $f_{\text{sync}} = 100\,\text{Hz}$, which resulted in an average time difference between each sync message of $\overline{\Delta t}_{\text{sync}} = (10.10 \pm 0.01)\,\text{ms}$ with a standard deviation of $\sigma_{\text{sync}} = (0.010 \pm 0.002)\,\text{ms}$. The response PDOs from the motion controller were sent after $\overline{\Delta t}_{\text{motor}} = (1.336 \pm 0.006)\,\text{ms}$, while the ADC sent its responses with a delay of $\overline{\Delta t}_{\text{sensor}} = (1.343 \pm 0.009)\,\text{ms}$. These values fluctuate with a standard deviation of $\sigma_{\text{motor}} = (0.025 \pm 0.006)\,\text{ms}$ and $\sigma_{\text{sensor}} = (0.03 \pm 0.01)\,\text{ms}$ [15]. The standard deviations indicate a fluctuation of the transmission times, while the request rate of the sync messages is fixed and only the response times of the ADC and the motion controller are unknown. Note that in this case, the term 'sensor' refers to the ADC and not the actual optical sensor.

5.1.1 Synchronization frequency of $f_{\text{sync}} = 100\,\text{Hz}$

To compare this with the newly installed ADC, 500 sync messages were examined with the same transmission frequency and also with a frequency of $f_{\text{sync}} = 1000\,\text{Hz}$. In both cases, as well as in J.Lämmel's analysis, the CAN messages and their respective timestamps were extracted from the monitoring via candump in the Linux shell. Figure 5.1 shows the

calculated time differences between each sync message as well as the referring histogram for $f_{\text{sync}} = 100\,\text{Hz}$. As in the previous analysis from [15], the time differences do not exactly match the expected value of $t_{\text{sync}} = 10\,\text{ms}$ but fluctuate around a larger average of $\overline{\Delta t}_{\text{sync}} = (10.077 \pm 0.003)\,\text{ms}$ with a standard deviation of $\sigma_{\text{sync}} = (0.043 \pm 0.003)\,\text{ms}$. Since the average time difference here is just 0.1 % smaller than the previous one, the sync messages are not sent significantly more precise. This delay with regard to the expected sync interval is potentially caused by processing times of the script that commands the sync messages, as the time is added on receiving the message. Additionally, the standard deviations show that the current sync intervals seem to fluctuate in a wider range than with the previous ADC. The standard deviation of the sync time difference is around four times larger than from the prior analysis, but does not interfere with other messages, since it is only 0.4 % of the time difference.

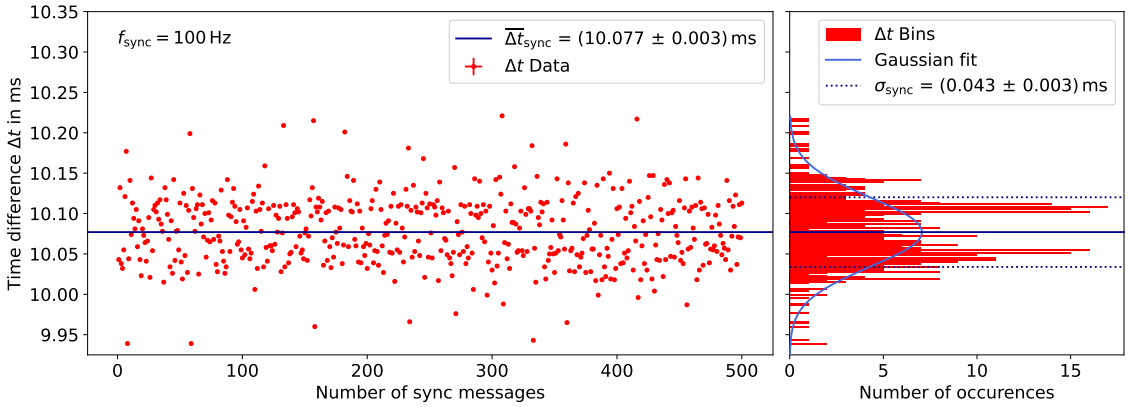

Figure 5.1: Diagram and respective histogram of the time difference between 500 sync messages. The synchronization rate is $f_{\text{sync}} = 100\,\text{Hz}$. The range of the data points were devided into 200 bins for the histogram.

The average response times as well as the respective histograms for both motor and ADC are found in Figure 5.2. It can be seen that not only the response times but also the standard deviations are smaller in comparison to the prior analysis. With $\overline{\Delta t}_{\text{motor}} = (1.261 \pm 0.003)\,\text{ms}$ and $\overline{\Delta t}_{\text{ADC}} = (1.266 \pm 0.001)\,\text{ms}$, both values are around 5 % smaller than the previously estimated response durations. The standard deviations for the response times of the motor and the ADC are in near proximity to the prior values, so that the fluctuation of the respective response times seemingly did not change.

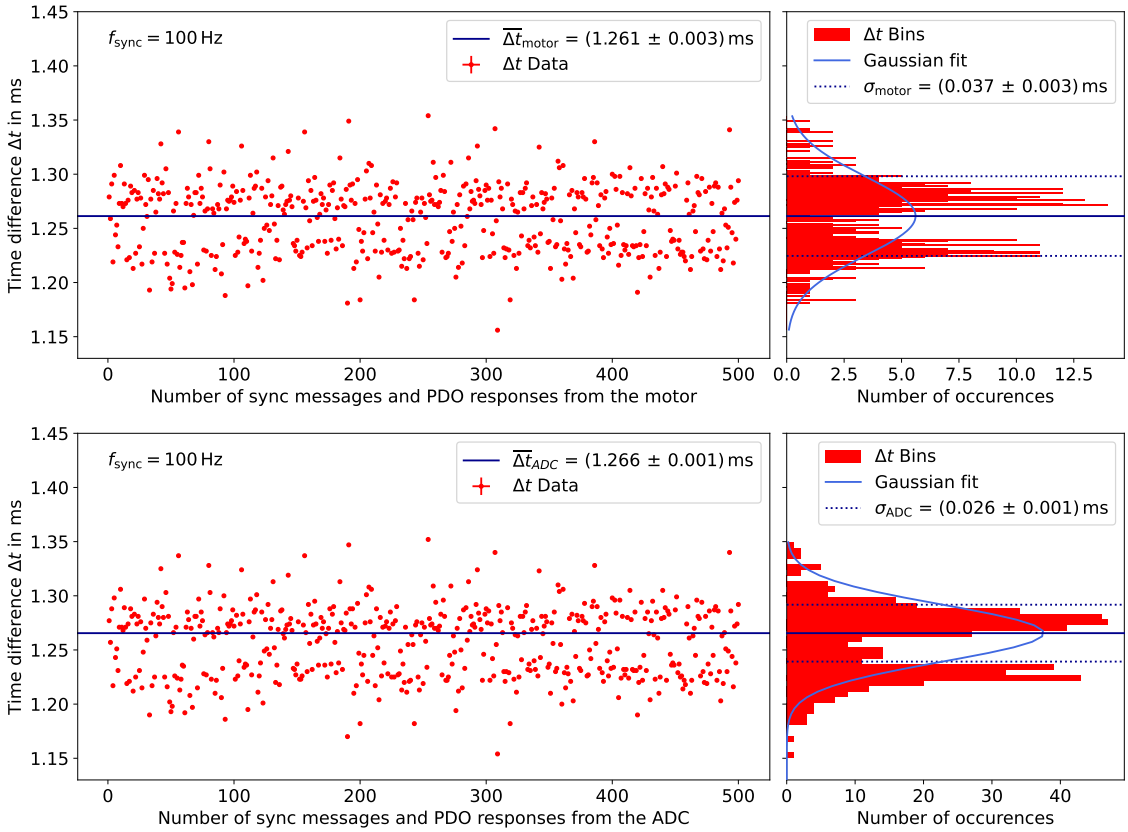

Figure 5.2: Diagrams and respective histograms, showing the PDO response times of the motor and the ADC to 500 sync messages. The synchronization rate is $f_{\text{sync}} = 100\,\text{Hz}$. The range of the data points were devided into 200 bins for the histograms.

5.1.2 Synchronization frequency of $f_{\text{sync}} = 1000\,\text{Hz}$

As already mentioned, the synchronization analysis was repeated with a sync frequency of $f_{\text{sync}} = 1000\,\text{Hz}$. In Figure 5.3, the time differences between the sync pulses are shown. The average time difference of $\overline{\Delta t}_{\text{sync}} = (1.0277 \pm 0.0007)$ is again larger than the expected time interval of $t_{\text{sync}} = 1\,\text{ms}$. The standard deviation of $\sigma_{\text{sync}} = (0.0131 \pm 0.0007)\,\text{Hz}$ is about 1.3 % of the average time difference and therefore three times larger than the ratio $\sigma_{\text{sync}}/\overline{\Delta t}_{\text{sync}}$ for $f_{\text{sync}} = 100\,\text{Hz}$. However, this deviation does not lead to a disturbance of the data transmission as the sequence of alternating sync messages and response PDOs is maintained with f_{sync}, except for the message duplications which are explained below.

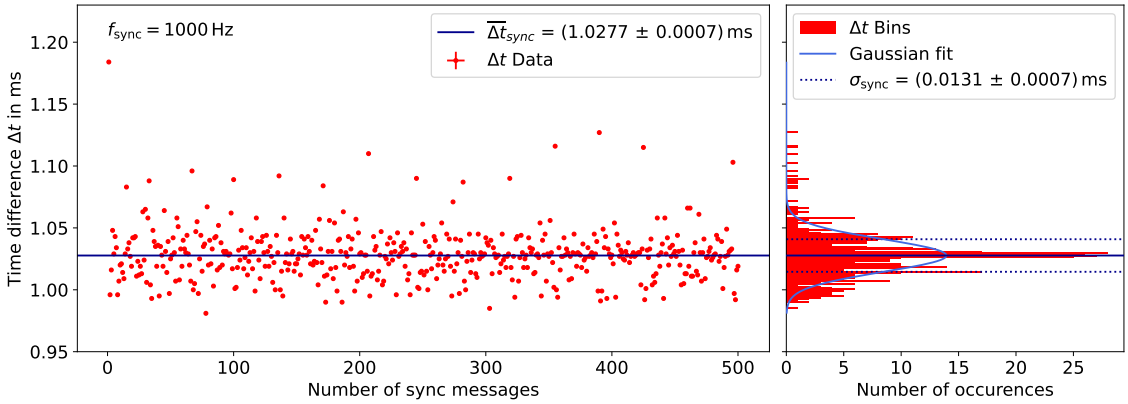

Figure 5.3: Diagrams and respective histogram, showing the time differences of 500 sync messages. The synchronization rate is $f_{\text{sync}} = 1000\,\text{Hz}$. The range of the data points were devided into 200 bins for the histograms.

The response times of the motion controller and the ADC can be seen in Figure 5.4. The average response times of $\overline{\Delta t}_{\text{motor}} = (0.203 \pm 0.002)\,\text{ms}$ and $\overline{\Delta t}_{\text{ADC}} = (0.202 \pm 0.002)\,\text{ms}$ are smaller to match the higher synchronization frequency. This is also why the fluctuations appear to be higher, since the standard deviations are almost 9 % of the respective response times. Looking at the raw values, however, the order of magnitude did not change. The fluctuations stay on the same absolute level, while they appear relatively larger compared to the smaller response times.

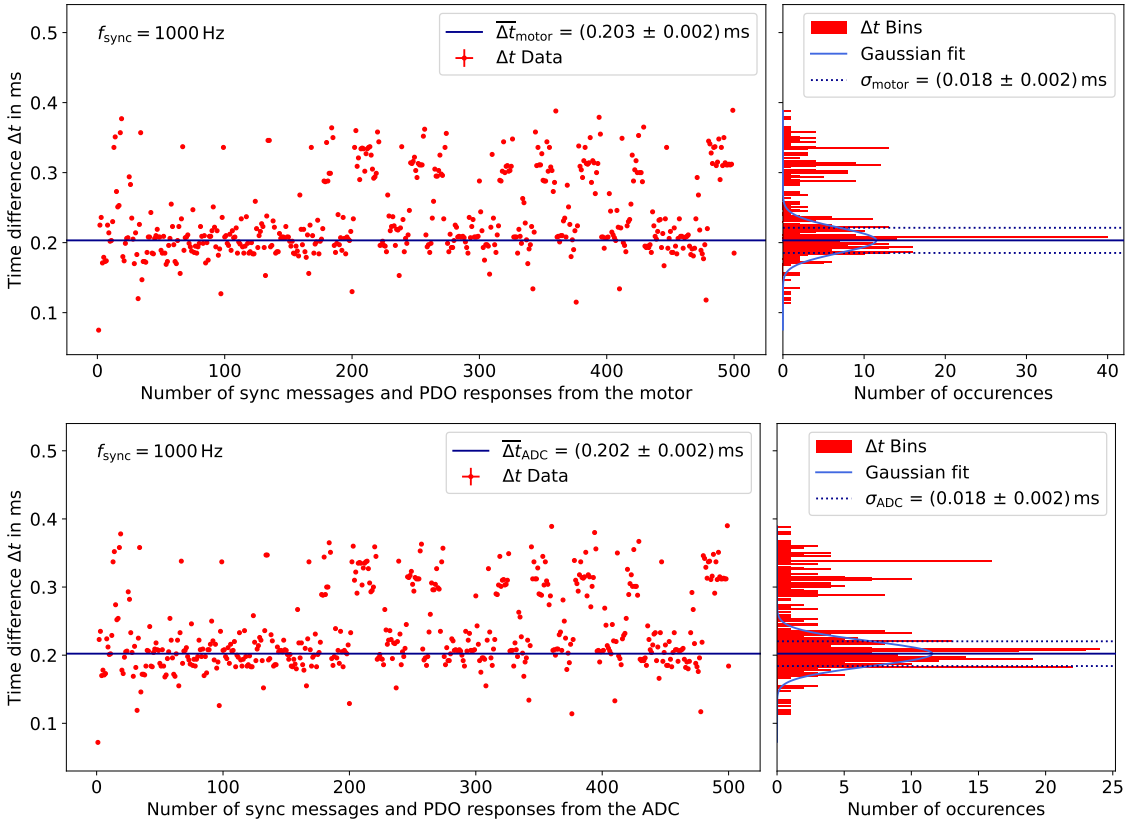

Figure 5.4: Diagrams and respective histograms, showing the PDO response times of the motor and the ADC to 500 sync messages. The synchronization rate is $f_{\text{sync}} = 1000\,\text{Hz}$. The range of the data points were devided into 200 bins for the histograms.

Important to add in case of the response times at $f_{\text{sync}} = 1000\,\text{Hz}$ is that some sync messages (below 4 % of all messages) were answered with two successive PDOs and then one following sync pulse was not answered at all. Considering the time difference of just a few microseconds between the two PDOs, it seems that the messages are duplicated, since a CAN message without the data field already takes 0.047 ms to be sent at a bitrate of 1 Mbit/s. In the analysis here, those points were skipped, since the algorithm for time difference estimation was implemented such that sync message and response PDO are always alternating. Including those samples would alter the analysis by calculating wrong time differences. However, even if this applies to only around 4 % of the sync messages sent, this behaviour is still undesired because the synchronization sequence gets lost in these points. Even though CAN bus is inherently robust, duplications and corruptions of CAN messages can appear due to intermittent network glitches which can occur especially at higher synchronization frequencies. It is therefore recommended to operate at lower synchronization frequencies or to change the PDO transmission to cyclic transmission which sends the PDO after a configured timer has elapsed.

5.2 Sampling of the ADC

In order to determine the wire tension, signal reproduction of the wire oscillations must be achievable with the ADC. To gain first impressions of its sampling, simple sine waves were generated by a frequency generator (evtl modell) that was connected to the analog inputs of the ADC. To imitate the oscillation frequencies of the anode and cathode wires, different frequencies f ranging from 80 Hz up to 270 Hz were generated with an amplitude of $A = \pm 4\,\text{V}$ and an offset of $C = 0\,\text{V}$. In addition to that, the sampling of the ADC was changed from synchronized to cyclic PDO transmission. The `main.py` program (see Listing 4.1) was not executed because network synchronization was not needed for these measurements. Only `candump` was used to pipe the PDOs from the ADC into a file.

The highest and lowest frequency sine waves that were measured are plotted and fitted in Figure 5.5, while the estimated frequencies f_{sin} are listed in Table 5.1. For each frequency, 4000 sample points were recorded, which is equivalent to a measurement duration of 4 s with a sampling rate of $f_{\text{S}} = 1000\,\text{Hz}$. Noticeable for the sine waves is that some samples fluctuate and do not lie on the fit curve. However, the aspect of interest for the WTTD is not the pure sampling accuracy of the wire oscillation, but rather its frequency reproduction. This considered, the estimated frequencies in the plots and the set frequencies of the signal generator correspond precisely, with deviations far below the maximum tolerable deviations from table 5.1.

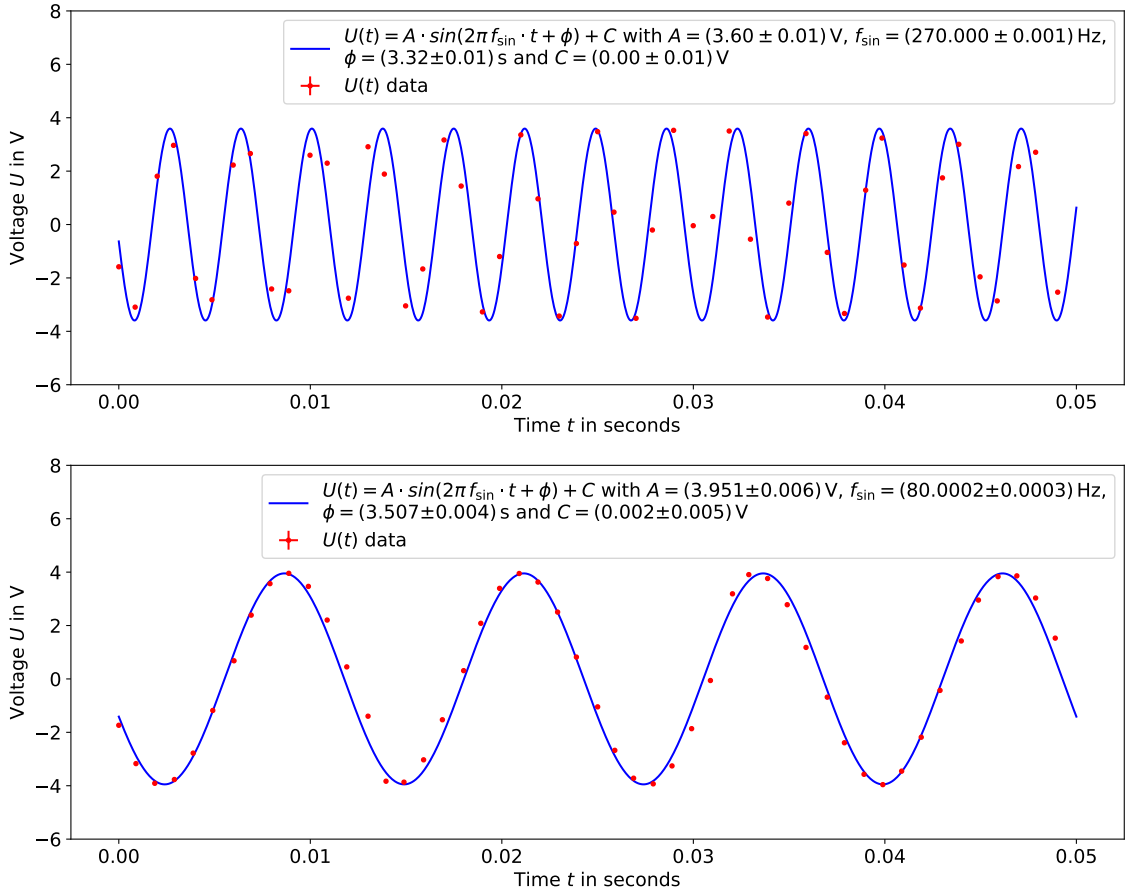

Figure 5.5: Data plots and respective fit curves of the sampled sine waves with $f = 270\,\text{Hz}$ (top) and $f = 80\,\text{Hz}$ (bottom). For graphical clarity, only the first 50 ms of the measurements are shown.

Since the amplitude of the wire oscillation drops exponentially, the oscillation subsides after a certain short duration and does not hold for the whole measurement duration. To analyze the frequency reproduction for shorter oscillation durations, the initial datasets were divided into intervals of 50 data points, which is equivalent to a duration of 50 ms. Then, the optimal parameters for each section were numerically calculated with ODR and the frequencies were collected inside a histogram. The average frequencies $\overline{f}_{\text{sin,sect}}$ as well as the standard deviations $\sigma_{\text{sin,sect}}$ are listed in Table 5.1 and the respective histograms for the 270 Hz- and 80 Hz-sine curves are given in Figure 5.6.

As can be seen for the 270 Hz-sine curve, even for smaller time intervals, the average frequency matches the expected frequency accurately. Additionally, the standard deviation of $\sigma_{\text{sin}} = (0.036 \pm 0.004)\,\text{Hz}$ is again much smaller than the maximum acceptable deviation for the anode wires in the chamber modules 1&3 (see Table A.1). However, for the 80 Hz-sine wave fits, a significantly larger standard deviation $\sigma_{\text{sin}} = (0.3 \pm 0.1)\,\text{Hz}$ is found. This also applies to the 100 Hz-sine wave, which has, in comparison to the higher frequency signals, a larger standard deviation. In this case, higher frequency signals refer to all sine curves with frequencies of and above 150 Hz, as their parameters are more precise due to smaller deviations.

The reason for this discrepancy derives from the combination of the function used for parameter calculation of the sections and the higher proximity of the amplitudes from higher frequency signals. The function was implemented such that for each section, it iterates over a given phase range with a given step width when handing over the initial parameter values for the ODR-fit. This is because the phase shift varies for different

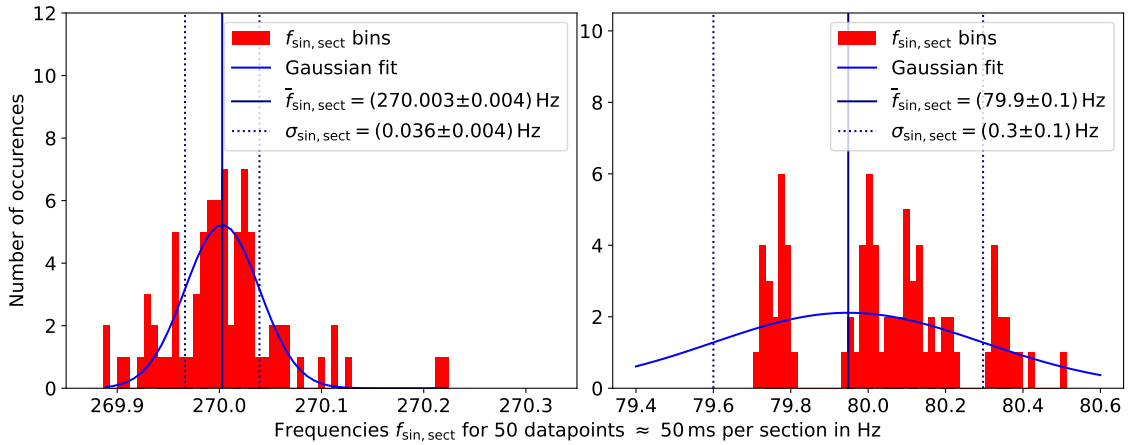

Figure 5.6: Histograms which gather the frequencies $f_{\mathrm{sin,sect}}$ estimated for each section consisting of 50 data points. For both histograms, the range of the accumulated frequencies from the repetitive fitting was segmented into 50 bins.

sections, unlike the amplitude, frequency and offset which remain the same. A constant initial phase shift for all sections would lead to strongly fluctuating frequencies, which in turn would alter this statistical analysis. However, when iterating over the phase-shift range, only the fit with the frequency closest to the expected frequency is retained. Furthermore, the imperfect sampling accuracy of the ADC causes some data points that are not aligning with the fit curve to lie within higher proximity of adjacent amplitudes. Thus, more different fit curves are created when iterating over the phase-shift range with more frequencies closer to the expected one. This effect applies especially for the higher frequency sine waves, which is why their standard deviations are smaller than those of the lower frequency signals.
All in all, the results of this section show that, even with lower sampling precision for larger frequency signals, the fundamental frequencies of the wire oscillations can be sampled and extracted sufficiently, unlike the ADC used in the prior setup [15].

f	$f_{\sin}$	$\overline{f}_{\sin,\mathrm{sect}}$	$\sigma_{\sin,\mathrm{sect}}$	$\sigma_{f,\max}$
270	270.0000 ± 0.0096	270.003 ± 0.004	0.036 ± 0.004	1.4
250	250.0070 ± 0.0011	249.999 ± 0.010	0.102 ± 0.010	1.3
200	199.9980 ± 0.0008	199.990 ± 0.006	0.053 ± 0.006	1.0
150	150.0001 ± 0.0006	150.025 ± 0.020	0.152 ± 0.020	0.8, 0.7
100	100.0003 ± 0.0004	100.116 ± 0.100	0.432 ± 0.102	0.5
80	80.0002 ± 0.0003	79.949 ± 0.129	0.348 ± 0.150	0.3

Table 5.1: Estimated frequencies and deviations from the measured sine waves with frequencies f. Also, the maximum deviation $\sigma_{f,\max}$ which leads to a wire tension deviation of 1 % was calculated with Equation A.6 after determining the corresponding wire length L with Relation 3.18. The maximum deviation for 80 Hz and 100 Hz oscillations were calculated with the parameters for the cathode wire, while the 200 Hz-, 250 Hz- and 270 Hz-oscillations were determined with the parameters of the anode wire. For 150 Hz, it was calculated for both types of wires (first value for anode and second for cathode wire). All values are given in Hz.

5.3 Measurement characteristics of sensor, preamplifier and low-pass filter

To examine the signal processing of the sensoric components besides the ADC, measurements with and without a tensed anode with a tension of $T_a = 0.5\,\mathrm{N}$ wire were taken to analyze the detected reflection from the wire, as well as the noise in different situations. The signal was passed to an oscilloscope (*PicoScope 6404E*), which additionally provides tools for signal analysis, such as mean calculation, minimum and maximum signal value, peak-to-peak height, etc. In Figure 5.7, an oscillation of the tensed anode wire was manually triggered through physical deflection of the wire. As explained before, physical contact is not desired because of the damage that could be inflicted on the wires and was only done since the air valve was not integrated yet.

The upper diagram shows the raw signal of the optical sensor, without any amplification. Evidently, the raw signal reaches a minimum peak of around $s = (-77.95 \pm 0.01)\,\mathrm{mV}$, but only for the beginning of the oscillation, as the later peaks only reach down to -40 mV to -50 mV. The dropping of the voltage originates from the measuring characteristic of the optical sensor. When no reflection is seen, the phototransistor within the sensor outputs full voltage at approximately $+12\,\mathrm{V}$ and dropping voltage once reflection is registered. This measurement profile of the sensor is also the reason why the positioning of the sensor above the wire is important. When being right above the center of the wire, one oscillation period results in two dips of the voltage signal because the wire moves two times through the focal point of the sensor. Thus, the measured signal has double the frequency of the actual oscillation frequency. Especially for the fundamental frequency of the anode wires in the chamber modules 1 & 3 (see Table 3.2), this leads to a signal with a higher frequency than half of the sampling frequency of the ADC and therefore, an alias in the power spectrum of the FFT. To prevent this, the sensor can be positioned such that the wire is on the edge of the visual field of the sensor. During wire oscillation, only one half of the period runs through the focal point, so that only one dip for one period is measured. The resulting signal then should have the exact frequency as the wire oscillation and no false frequencies should be displayed by the FFT.

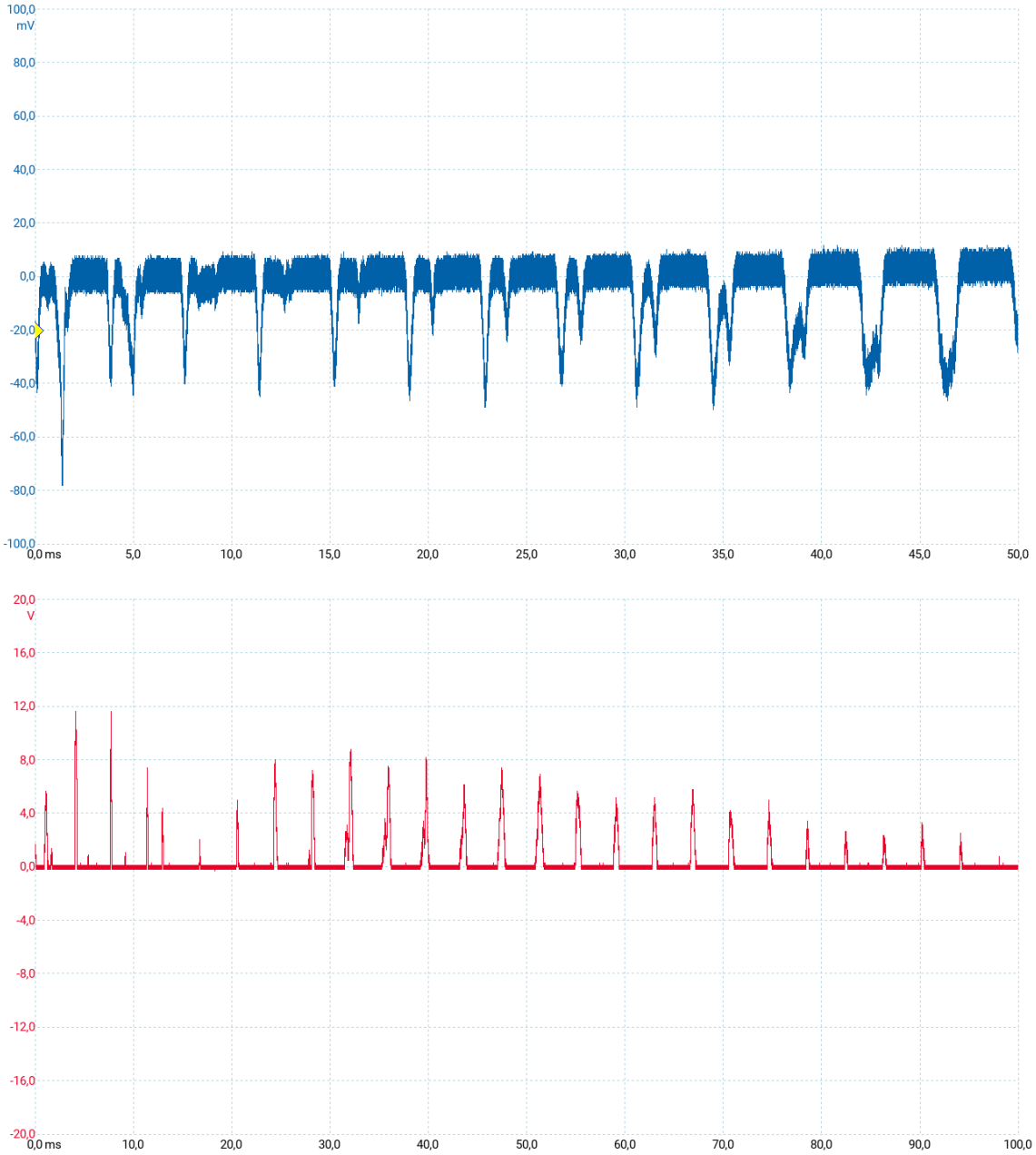

Figure 5.7: Signal of a manually triggered anode wire oscillation from the optical sensor only (blue) and the added preamplifier (red), with the time on the abscissa and the voltage on the ordinate. The raw sensor signal is given with AC coupling and the amplified signal with DC coupling. Note that the diagrams show different wire oscillations and have different axis scales to ensure a clear view of the signals.

The noise of the raw signal is displayed in Figure 5.8 (top) and has an amplitude of $n = (4.7 \pm 0.4)\,\mathrm{mV}$ resulting in a signal-to-noise ratio (SNR) of $|s|/n = 17 \pm 1$. Besides that, also the noise emerging when the motion controller is active has to be considered in the present setup, even though it is planned to be shielded by the housing of the motion controller and the sensor. During unshielded operation of the motor, the noise shown in Figure B.2 in Appendix B is $n_\mathrm{m} = (54 \pm 4)\,\mathrm{mV}$. Compared to the oscillation signal, this results in a SNR of only around $|s|/n_\mathrm{m} = 1.4 \pm 0.1$.

To increase the oscillation signal, a preamplifier is implemented that amplifies the initial signal of the sensor. It also inverts the characteristics of the sensor because it has no offset and responds with rising voltage when reflection is registered, up to a saturation

of +12 V. A manually triggered wire oscillation can be seen in Figure 5.7 (bottom). In this case, the peaks of the amplified signal range from 3 V up to $s_{\text{amp}} = (11.7 \pm 0.3)\,\text{V}$. Surprisingly, the noise characteristic for both the normal noise of the baseline ($n_{\text{amp}} = (3.9 \pm 0.3)\,\text{mV}$) and the noise created by the motor ($n_{\text{amp,m}} = (42 \pm 4)\,\text{mV}$) is slightly reduced when adding the preamplifier, as shown in Figures 5.8 (bottom) and B.2 (see Appendix B). One possible reason is that the noise is captured via the ground potential of the ADC. Anyhow, this results in a significantly larger SNR of around $s_{\text{amp}}/n_{\text{amp,m}} = 280 \pm 30$. Important to note is that during the wire oscillation measurement, the motion controller is only active to open and close the air valve because the valve is connected to its digital output. After triggering the oscillation, the motion controller remains idle and thus the oscillation signal is presumably not affected by its noise, leading to an even higher SNR.

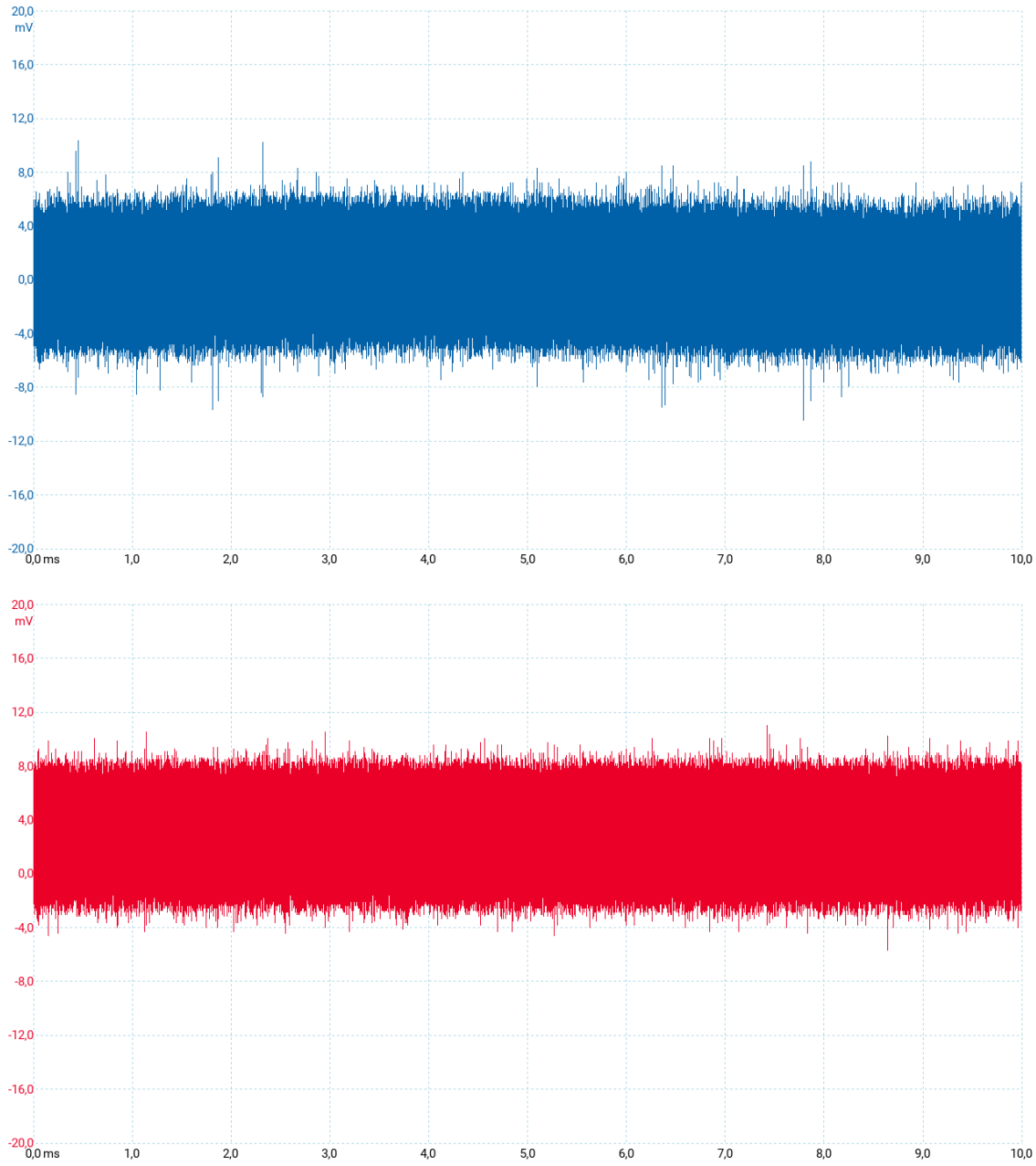

Figure 5.8: Noise of the optical sensor without (blue) and with (red) the preamplifier. Again, the raw signal is given with AC coupling and the amplified with DC coupling.

Nonetheless, the integration of the preamplifier raises another phenomenon. When measuring reflection, the amplified signal possesses different noise frequencies, which are shown in Figure 5.9 (top). The origin of these frequencies cannot be identified exactly, since they could be caused by any component connected to the electrical circuit of the sensor system.

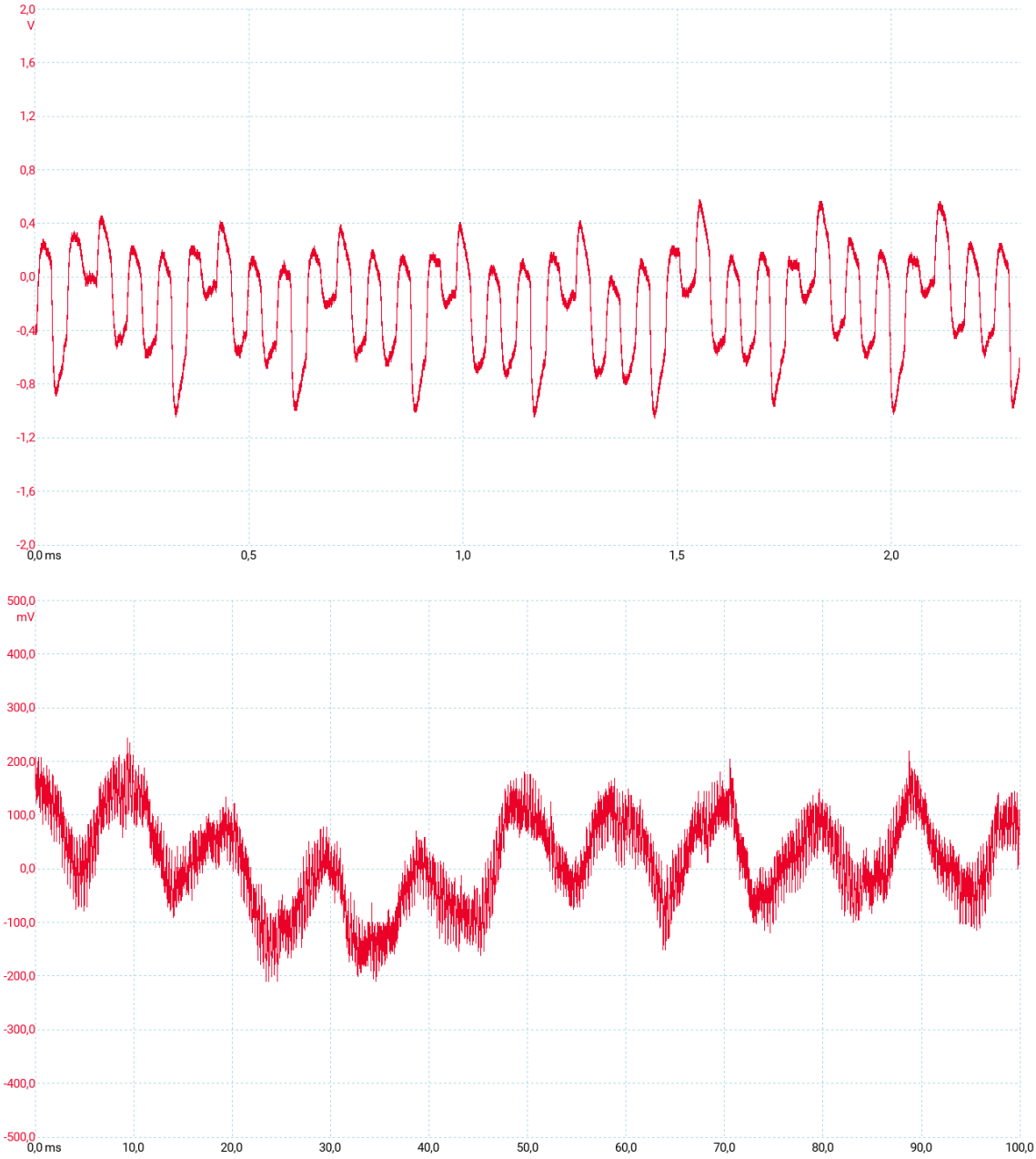

Figure 5.9: Noise of the preamplifier without (top) and with (bottom) low-pass filter, when registering reflection. The diagrams show different axis scales to establish a clear view of the signals.

To suppress those frequencies, an additional low-pass filter is implemented to the sensor system. Its influence on a measured signal is shown in Figure 5.9 (bottom). As can be seen, higher frequencies are filtered out, but the signal still shows a frequency of approximately 100 Hz. Unfortunately, this is within the order of magnitude of the oscillation frequencies of the cathode wires (see Table 3.2), so it is expected to occur as a peak in the frequency spectrum of the FFT. However, this noise frequency does not correspond exactly to any

expected fundamental frequencies of the wires (see Table 3.2) and, furthermore, the non-filtered signal would most likely be visible in the frequency spectrum anyhow due to the aliasing effect. Additionally, the reflection noise without the low-pass filter has a much higher magnitude of around $n_{\mathrm{amp,r}} = (0.7 \pm 0.1)\,\mathrm{V}$, while the filtered noise has an amplitude of just $n_{\mathrm{amp,f}} = (0.13 \pm 0.02)\,\mathrm{V}$. This makes the filter especially helpful for measuring the wire oscillation, since its amplitude can be just a few volts high, as can be seen in Figure 5.7

5.4 Focal point and reflection measurement of the optical sensor

After improving the SNR by including the preamplifier and the low-pass filter, further investigations regarding the visibility of the wires and their oscillations are executed. The reflection of an anode as well as a cathode wire was measured for different distances d between the reflective sensor and the respective wire. With the test function `scan_pos()`, the photosensor was moved over a distance of 2 cm above the wire while the ADC measured its voltage output.

Even if the reflection signal of the wires was already hinted at in the previous section, some signals are depicted exemplarily in Figure 5.10. Additionally, the maximum voltage value U_{max} for each distance between 1 mm and 6 mm is given in Figure 5.11. As can be seen, the maximum voltage for the anode wire rises for higher distances d_{a}, peaking at $d_{\mathrm{a}} = (3.750 \pm 0.001)\,\mathrm{mm}$, while the output for the cathode wire reaches the saturation of the ADC at almost every distance d_{c}. This discrepancy most likely appears because of, firstly, a slight displacement of the photosensor, which was not positioned perpendicularly towards the wires, causing the phototransistor to detect less reflected light. In Section 5.6 e.g., a reflection signal will be shown that reaches 10 V even for a distance of $d_{\mathrm{a}} = (5.500 \pm 0.001)\,\mathrm{mm}$ and a lower luminosity of the photodiode. Secondly, the more than three times larger radius of the cathode wire (see Table 3.2) enables it to reflect more light. Thus, even with the displacement of the sensor, the cathode wire reflects sufficient amounts of light for the signal to reach maximum voltage.

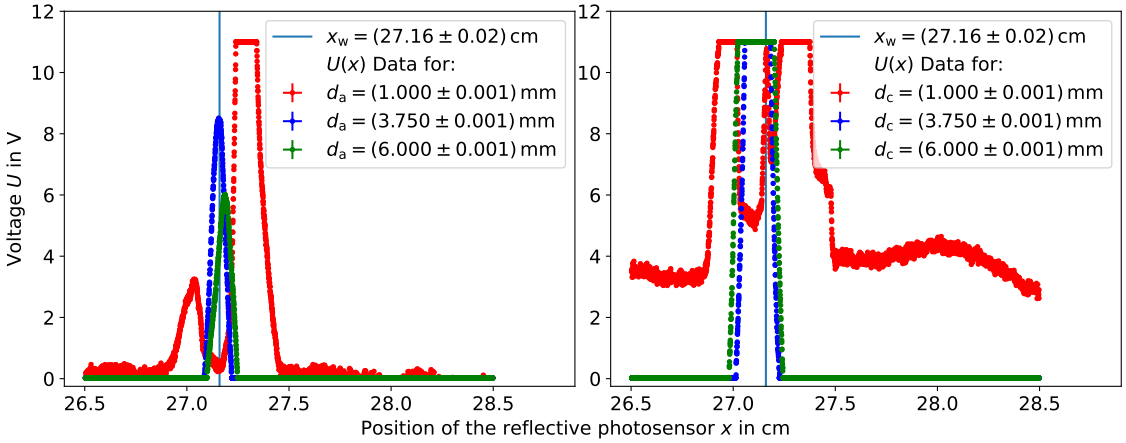

Figure 5.10: Reflection of the anode wire (left) and the cathode wire (right) at different distances d_{a} and d_{c}. The actual position of the wire is at $x_{\mathrm{w}} = (27.16 \pm 0.02)\,\mathrm{cm}$.

Conspicuous for the anode wire is that at lower distances, two peaks occur which are reduced when increasing the distance, until they completely vanish at $d_{\mathrm{a}} = (3.500 \pm 0.001)\,\mathrm{mm}$. Simultaneously, between those two peaks, a third peak representing the actual position x_{w} of the wire emerges and grows. This effect also appears for the cathode wire, but due to its overall stronger reflection intensity, the peak at x_{w} is already almost at

the saturation voltage, even for $d_c = (1.000 \pm 0.001)$ mm. This behaviour indicates that for distances far below the manufacturer stated focal point of the sensor $d_f = 6$ mm (see Section 4.1), the wire reflects the infrared light at different locations and does not reflect them into the phototransistor when centered underneath the sensor. Most likely, the photons are emitted in a cone shape towards the focal point, which could lead to such an effect.

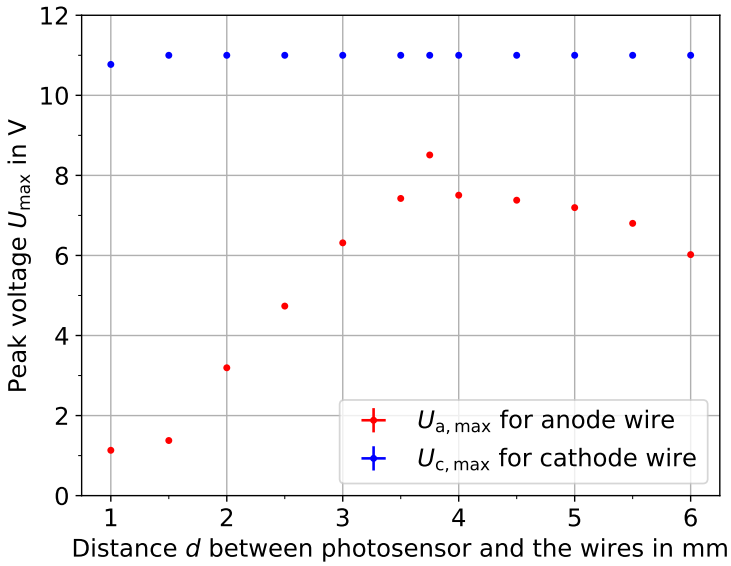

Figure 5.11: Maximum voltage U_{max} for each distance d_a between the sensor and the anode wire (red) and d_c between the sensor and the cathode wire (blue). Note that U_{max} was selected in the uncertainty range of x_w.

Overall, positioning the photosensor at distances below $d = 3.5$ mm is not recommended because, firstly, the reflection measurements indicate uncontrolled reflection which leads to a potentially lowered measurement stability. Secondly, the air valve is located at a lower level than the sensor, creating a higher risk of physically contacting the wires at lower distances when moving across the wire plane.

Important to note is that the saturation voltage of the ADC (±10 V, see Section 4.1) is originally outputted as a negative voltage of -32.768 V. Since the highest voltage value measured from the data is 10.999 V, it is assumed that the saturation output is triggered when the signal exceeds 11 V. For this reason, the data points containing the negative saturation value were changed to be 11 V. Not only does that lead to a clearer view of the signals, but it also ensures correct frequency identification by the FFT. Eventually, this replacement needs to be included in the process of determining the wire tension, or the output of the photosensor must be regulated to stay below the saturation voltage of the ADC.

5.5 Wire oscillations

In this section, the wire tension of an anode and cathode wire is determined by the method presented in this thesis. The wires were stretched by soldering one end to the edge of a 6 cm tall iron block and attaching a weight to the other end, which hangs down over the edge of an additional iron block, placed at the edge of the laboratory table. Via a scale, the weight force was determined to equal the respective wire tensions of $T_a = 0.5$ N and $T_c = 1$ N. For the air blast that triggers the wire oscillation, a valve was added on the sensor carriage next to the sensor. With a hose, the valve was connected to the pneumatic air supply of the laboratory, which was set to an air pressure of 8 bar. The photosensor was positioned with a distance of $d_a = (3.750 \pm 0.001)$ mm and $d_c = (6.000 \pm 0.001)$ mm above the respective wire. Before the oscillation measurements were started, the sensor

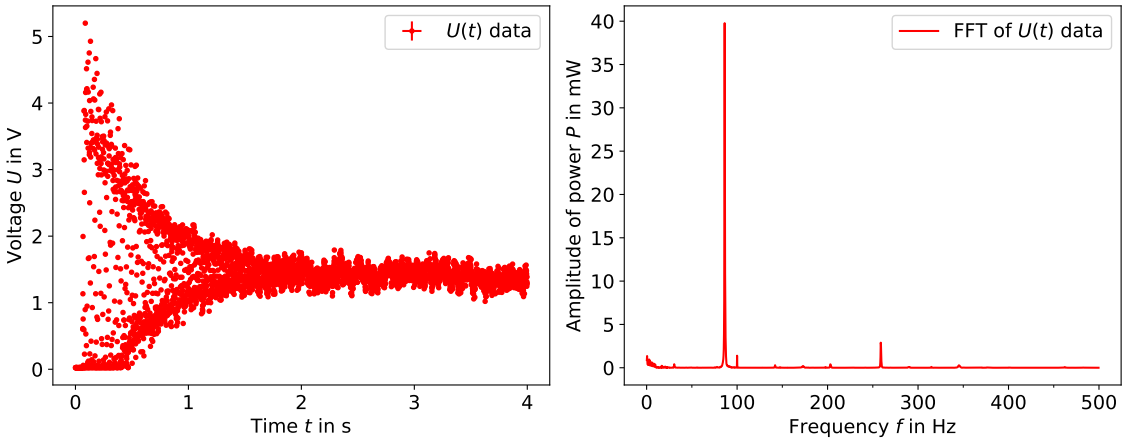

Figure 5.12: Measured wire oscillation in the time domain (left) and the respective power spectrum of the FFT (right) for a cathode wire with length $L = (96.00 \pm 0.02)\,\mathrm{cm}$.

was positioned such that the wires were on the edge of the visual field of the sensor to ensure frequency integrity of the signal.

The measurement of the wire oscillation is executed via the function `measure_oscillation()` which activates the valve and starts the transmission of the PDOs of the ADC right after. The measurement lasts for a duration of $t_\mathrm{S} = 4\,\mathrm{s}$ to achieve a sufficient frequency resolution of the FFT in order to keep the uncertainty of the wire tension below the desired limit of 1 % (see Appendix A). Additionally, the PDOs of the ADC are transmitted in cyclic mode every $\Delta t_\mathrm{S} = 1\,\mathrm{ms}$ because the position information from the motion controller is not needed when measuring the wire oscillation.

The voltage values of a cathode wire oscillation are exemplarily plotted in Figure 5.12 (left), together with the respective FFT which is calculated on the right-hand side of the same figure. As can be observed, there are three major peaks visible in the FFT. The first and also the one with the highest magnitude is located at $(86.25 \pm 0.25)\,\mathrm{Hz}$ and indicates the fundamental frequency of the cathode wire from the TRD chamber modules 1 & 3 (see Table 3.2). The second peak at $(100.00 \pm 0.25)\,\mathrm{Hz}$ resembles the previously mentioned noise frequency that occurs when the sensor registers reflection. The third peak is located at $(258.76 \pm 0.25)\,\mathrm{Hz}$ which can be classified as a higher harmonic of the fundamental frequency since it is three times larger. Important to note is that the height of the peak for the fundamental frequency varies, especially between the anode and cathode wire. For the anode wire, the peaks are generally smaller and sometimes even smaller than the noise peak. Therefore, the peak for the fundamental frequency cannot be selected as just the first peak in the FFT in any case and needs to be distinguished from the noise peak.

The wire oscillations were repeated 15 times for each of the different wire lengths L. The average frequencies $\overline{f}$ and their standard deviations $\sigma_{\overline{f}}$ of the repeated measurements are plotted in Figure 5.13, together with the expected fundamental frequencies f_exp that lead to the respective wire tensions T_a and T_c. The resulting wire tensions $\overline{T}_\mathrm{a}$ and $\overline{T}_\mathrm{c}$ calculated with $\overline{f}$ are additionally depicted in Figure 5.14. Evidently, the estimated average frequencies as well as the wire tensions deviate strongly from the expected values for both types of wires. Even the closest average wire tensions $\overline{T}_\mathrm{a} = (0.4912 \pm 0.0002)\,\mathrm{N}$ ($L = (105.00 \pm 0.02)\,\mathrm{cm}$) and $\overline{T}_\mathrm{c} = (0.9875 \pm 0.0004)\,\mathrm{N}$ ($L = (96.00 \pm 0.02)\,\mathrm{cm}$) deviate more than 1 % from the expected wire tensions. Furthermore, the form of the relation between the fundamental frequency and the wire length $f_0 \sim 1/L$ is hardly recognizable, especially in case of the anode wire. As can be seen in Figure 5.13, many estimated frequencies for longer wires are larger than the frequencies of shorter wires. Despite that, the precision of the estimated frequencies and tensions is sufficient, as their standard deviations, given as

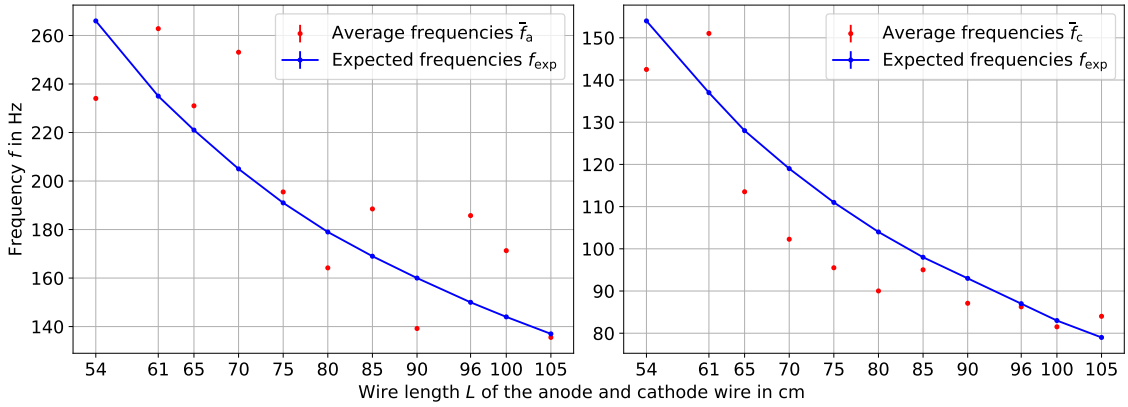

Figure 5.13: Average frequencies of 15 wire oscillations of the anode wire $\overline{f}_a$ and the cathode wire $\overline{f}_c$ against the wire length L. Also given are the expected frequencies f_{exp} for each wire length, calculated with Formula 3.18.

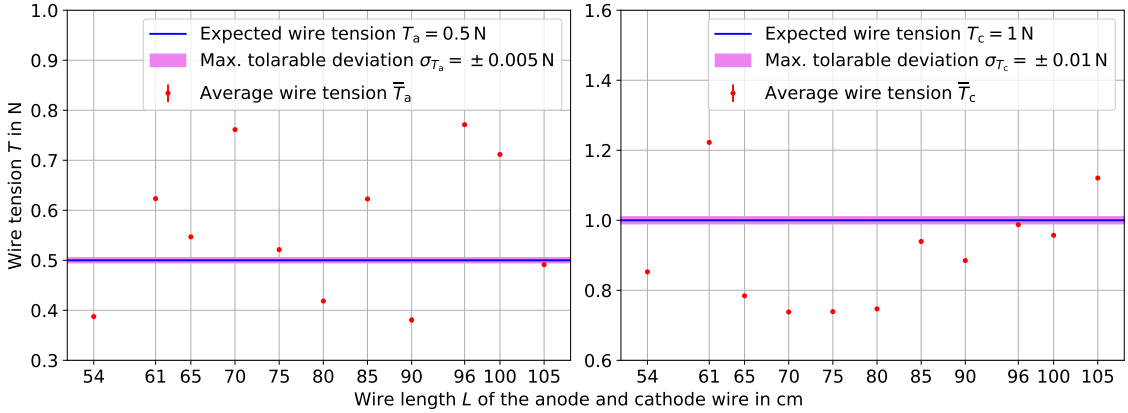

Figure 5.14: Average wire tensions $\overline{T}$ calculated with $\overline{f}$ through the formula 3.18. Also given are the expected wire tension T_a and T_c with the maximum tolarable deviations σ_{T_a} and σ_{T_c} (see Appendix A). Note that $\overline{T}_a$ at $L = (105.00 \pm 0.02)$ cm and $\overline{T}_c$ at $L = (96.00 \pm 0.02)$ cm are not within the maximum tolarable deviation region, even if they appear so.

their uncertainties in the diagrams 5.13 and 5.14, are always within the 1 %-limit of the maximum tolerable deviations.

These results do not satisfy the demands of the WTTD, but determining one crucial reason for this appears to be difficult, particularly because the oscillations were simultaneously checked with an oscilloscope. Through visual judgment, the estimated oscillation frequency of the displayed signal approximately matched the frequencies given in Figure 5.13, so that an incorrect sampling of the ADC can be excluded. Because the weights which tensed the wires were precisely measured and adjusted to equal the desired wire tensions, one might even assume that the wires certainly did not oscillate with the expected frequencies. Further scrutiny of these discrepancies is necessary, which might have been caused by multiple aspects.

For example, the previously explained attachment of the wires to the iron blocks permits friction between each end of the wires and the surface of the blocks, which could disturb the oscillation measured, although the proportion of the wire length affected by this friction is below 2 cm. Furthermore, the mounting might cause the wire to be twisted, e.g. due to a rotation of the hanging weight. In combination with damaged wire surfaces,

this might lead to an inhomogeneous reflection profile of the wire. Since the surfaces of the wires were not directly checked, e.g. via a microscope, one can only assume that damage or even deformation of the wires occurred during their attachment because they were physically contacted with skin, tables, dust and other objects. Nevertheless, their surface should be checked to ensure the radial symmetry of the wires and exclude irregular reflection. Moreover, the opening time of the air valve was increased from 13 ms (as in other projects for wire tension measurements found [11, 18, 15]) to 50 ms, which might hinder the wire from reaching the harmonic motion. It was increased due to difficulties of hitting the wire with the air blast. A higher opening time seemed to deflect the wire stronger and more frequently but has to be reverted back to the original value eventually.

As the deviations of the estimated wire tensions in this section might be caused by the given factors, the other aspects of the sensor system mostly prove themselves to fulfill the tasks of the WTTD so far. The data transmission as well as the sampling of the ADC is fast enough to measure even the highest expected fundamental frequency of the anode wires in the chamber modules 1 & 3 (see Table 3.2). Additionally, the preamplifier and the low-pass filter achieve signal amplification of up to 12 V, as well as a sufficient SNR. However, the reflective and light-emitting characteristics of the photosensor need further examination, especially regarding the reflection when measuring the wires above the cathode pad plane of the ROCs. Therefore, the next section presents additional reflection measurements of the wires with a piece of the cathode pad plane underneath them.

5.6 Reflection measurements with the cathode pad plane

The inclusion of the cathode pad plane derives from the fact that the wire tension is measured between the attachment of the wire planes during the production of the ROCs, as explained in Section 3.2. Since the anode wire plane is placed 3.5 mm above the cathode pad plane, a piece of the cathode pad plane was lifted to this distance underneath the anode wire. As in the reflection measurements before (see Section 5.4), a distance of 2 cm was scanned above the wire. The sensor output can be seen in Figure 5.15. Evidently, the reflection of the cathode pad plane is too strong so that the sensor outputs full voltage over the whole distance. Thus, the location and the tension of the wires cannot be determined when above the cathode pad plane. Even for higher distances d_a the reflection of the cathode pad plane fully overrides that of the anode wire. It is essential to solve this problem because otherwise, the photosensor proves to be unsuitable for the purpose of the WTTD.

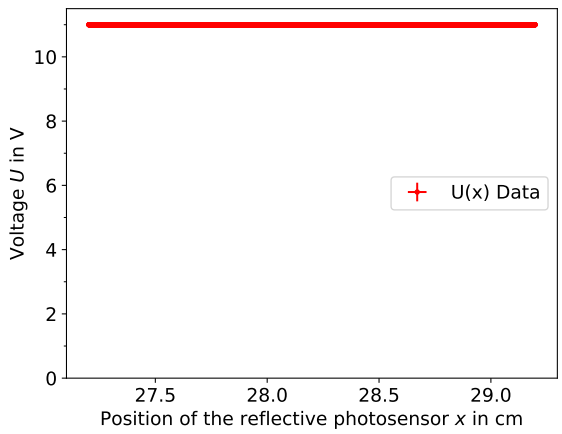

Figure 5.15: Reflection of the cathode pad plane measured with the photosensor being $d_a = (3.750 \pm 0.001)$ mm above the wire.

The concept to solve this problem was to add another RPR-220 photosensor on the

carriage such that there is a certain angle between the two sensors. Only the phototransistor of the perpendicular sensor and the photodiode of the angled sensor are fed by a supply voltage so that the angled sensor solely emits light towards the wire, while the perpendicular sensor detects the reflection. This way, only the reflection of the wire should be measurable since the wires have radial symmetry, while the cathode pad plane reflects the light away from the phototransistor. However, the light-emitting diode (LED) cannot be oriented at an arbitrary angle. On the one hand, angles that are too low cause the light to still be reflected from the cathode pad plane into the phototransistor. On the other hand, the LED physically hits the wire plane when the angle is too large.

This method was tested again via a position scan for different angles, as can be observed in Figure 5.16. For the measurements with $\alpha = (45 \pm 0.4)\,^\circ$ and $\alpha = (55 \pm 0.4)\,^\circ$, both wires cannot be located because only the reflection of the cathode pad plane can be measured. At $\alpha = (65 \pm 0.4)\,^\circ$, the phototransistor does not detect the reflected light from the cathode pad plane any further but is able to measure the reflection of the wire instead. At larger angles, no reflection is caught at all with the anode wire, while the cathode wire is still clearly visible. Again, the higher reflectivity of the cathode wire, due to its larger radius, leads to a wider range of angles for which the cathode wire can be located.

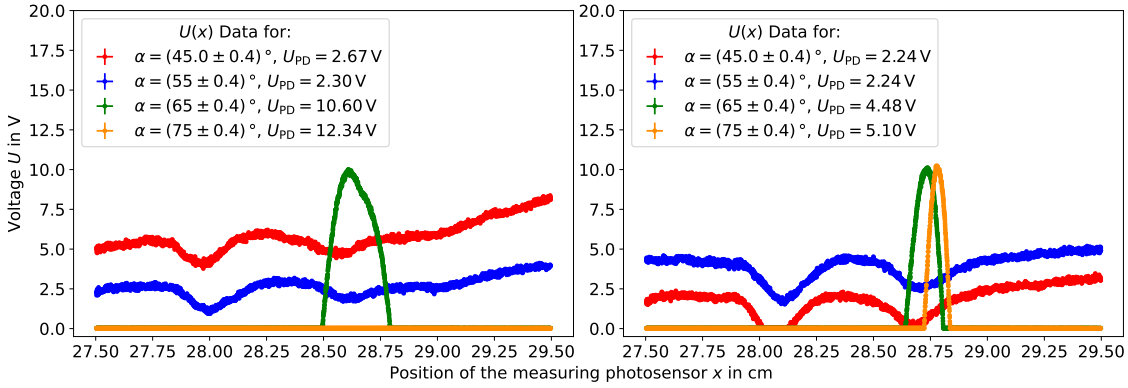

Figure 5.16: Reflection of the anode (left) and cathode (right) for different angles α between the light emitting and the light measuring sensor. The luminousity of the light emitting sensor was regulated through its supply voltage U_{PD}.

Overall, this method proves to be able to separate the reflection of the wire from that of the cathode pad plane. However, the supply voltage for the phototransistor and the LED was separated, which proves to be important, especially regarding the wire pitch in the wire planes of 2.5 mm. As the reflection peaks for the cathode wire in Figure 5.16 (right) show, a supply voltage for the LED of only $U_{\mathrm{PD}} = 4.48\,\mathrm{V}$ provides a sufficient intensity of the infrared light for the peaks to almost reach maximum output. When increasing the supply voltage, not only the height but also the width of the reflection peaks grow. After reaching maximum output, the peaks start forming plateaus, which increase in width for larger supply voltages. If a certain voltage U_{PD} is surpassed, the width of the plateaus might exceed the wire pitch, making it impossible for the wires to be located within the wire plane. Therefore, the LED voltage must be tuned directly in order to regulate the luminosity of the infrared light and the intensity of the reflection.

Chapter 6

Conclusion and Outlook

In order to maintain equally distributed charge amplification within the readout chambers of the CBM TRD, the mechanical tension of the anode and cathode wires needs to prevent them from sagging due to gravitational and electrostatic forces and thus altering the shape of the electric field within the ROCs. To ensure correct and precisely tensed wires, their tension should be checked during the production of the readout chambers. This is achieved by the WTTD, which examines the wire tension contactlessly to mitigate the risk of damaging the wires and operates fully automated for higher time efficiency.

The measurement is done by a reflective photosensor, which detects reflected light emitted by its photodiode. It is mounted onto a carriage that can be moved by a motor along the linear drive. Once the photosensor is positioned above a wire, an air blast from an air pressure valve triggers a wire oscillation. Oscillating through the focal point of the sensor, the reflection changes periodically with the frequency of the wire oscillation. By measuring the vibration signal and performing a Fast Fourier Transformation, the oscillation frequency of the wire can be determined and used to calculate the wire tension.

This thesis explains the fundamental concepts of the WTTD, including the working principle of all components, the structure and communication of its local network established via a Controller Area Network (CAN) and further Python software implementations. Besides that, new sensoric modules were commissioned and investigated regarding their suitability for the task of the WTTD. The speed of the data transmission in the local network and the 1 kHz sampling rate of the ADC could be verified to measure even the highest fundamental frequencies of the anode wires in the TRD chamber modules 1 & 3 successfully. Furthermore, the signal output of the photosensor was analyzed and enhanced with a preamplifier and a low-pass filter, achieving a signal-to-noise ratio of at least $s/n = 247$.

Even though the reflection of the cathode pad plane beneath the wires was initially overriding that of the wires, a solution could be found by altering the relative positioning of the light-emitting diode and the light-detecting phototransistor. Also, the width of the reflection peaks can be kept sufficiently low through regulation of the luminosity of the light-emitting diode, indicating correct and accurate localization of successive wires with a wire pitch of 2.5 mm.

In conclusion, the basic characteristics of the sensoric components prove to be suitable for the WTTD, although currently unexplained deviations remain in wire tension test measurements. Possible reasons for this, e.g. the mounting of the test wire must be identified. Moreover, measurements closer to the final operation of the WTTD should be executed, including the localization of wires in a wire plane, or the oscillation frequency of wires attached to a transfer frame. Furthermore, the housing of the sensor modules needs to be adapted to the alternative orientation of the photosensors to ensure correct detection of the wires above the cathode pad plane of the ROCs. Besides that, the data

output of the software implementations should be revised to be included in a protocol summarizing the data of all test procedures for the CBM TRD, which is aimed at in an ongoing master thesis project by H. Olbring.

Appendix A

Uncertainties

For uncertainty calculation of all measurable quantities during the experimental investigations, the guidelines of the "Guide to the Expression of Uncertainty in Measurement" [3] were applied.

The uncertainties of digitally measured values $u_{\mathbf{d}}$ were determined with the rectangular distribution, using the interval $s_{\mathbf{d}}$ between the ± 0.5 limits of the smallest digit displayed by the measuring device:

$$u_{\mathrm{d}} = \frac{s_{\mathrm{d}}}{2\sqrt{3}}. \tag{A.1}$$

For analogue values, the uncertainty u_{a} is calculated by the triangular distribution and the interval between the smallest scale increment s_{a}:

$$u_{\mathrm{a}} = \frac{s_{\mathrm{a}}}{2\sqrt{6}}. \tag{A.2}$$

The total uncertainty of a quantity u_{tot}, which has contributions of n different uncertainties u_1, u_2, etc. is calculated by the direct combination of each contribution:

$$u_{\mathrm{tot}} = \sqrt{u_1^2 + u_2^2 + \ldots + u_n^2} \tag{A.3}$$

Furthermore, quantities Y which are not directly measured, but determined through a relation between n measurable quantities X_{i} ($\mathrm{i} = 1, 2 \ldots n$) have their uncertainty estimated by the indirect Gaussian uncertainty propagation:

$$u_Y = \sqrt{\left(\frac{\partial Y}{\partial X_1} \cdot u_{X_{\mathbf{1}}}\right)^2 + \left(\frac{\partial Y}{\partial X_2} \cdot u_{X_{\mathbf{2}}}\right)^2 + \ldots + \left(\frac{\partial Y}{\partial X_{\mathrm{n}}} \cdot u_{X_{\mathbf{n}}}\right)^2} \tag{A.4}$$

with the uncertainties of the measurable quantities $u_{X_{\mathrm{i}}}$. The uncertainties from quantities which were obtained through data fitting were calculated by the ODR package from SciPy, weighting the uncertainties with the total deviation from the fit.

Regarding the wire tension within the TRD chambers, it should be estimated precisely by the WTTD. Therefore, a maximum tolerable deviation from the wire tension of 1 % is desired [15]:

$$\frac{u_{\mathrm{T}}}{T} \leq 0.01. \tag{A.5}$$

with u_{T} being the uncertainty of the wire tension. Since it is calculated over the fundamental frequency f_0 of the wires, the uncertainty is estimated via the Gaussian error propagation A.4 of the Relation 3.18 and the deviation of the fundamental frequency u_{f_0}:

$$u_{\mathrm{T}} = \frac{\partial T}{\partial f_0} \cdot u_{f_0} = 8\pi\rho f_0 L^2 r^2 \, u_{f_0}. \tag{A.6}$$

Applying Condition A.5 to the formula above and rearranging it, the maximum acceptable deviations for the fundamental frequencies in the different chamber modules can be determined, as given in table A.1.

	Module type 1 & 3	Module type 5 & 7
$u_{f_0,\text{anode}}$	1.3 Hz	0.8 Hz
$u_{f_0,\text{cathode}}$	0.8 Hz	0.4 Hz

Table A.1: Maximum tolerable deviations of the fundamental frequencies of the electrode wires in the given chamber modules (see table 3.2). Calculated with Formula A.6 and A.5.

Appendix B

Component housing

The motion controller as well as the sensoric components of the WTTD are planned to be placed inside individually designed housings. Not only do the housings provide protection for the components and a clean arrangement, but they shall shield the noise measured by the photosensor when the motion controller is active.

The noise originating from the motor is shown in Figure B.2. As already mentioned in section 5.3, the noise signals have an amplitude of $n_{\mathrm{m}} = (54 \pm 4)\,\mathrm{mV}$ and $n_{\mathrm{amp,m}} = (42 \pm 4)\,\mathrm{mV}$. Furthermore, these amplitudes do not change when varying the velocity of the sensor carriage. Although the SNR is sufficiently high (see Section 5.3) to measure wire oscillations even if the motor is active, e.g. because it controls the air pressure valve, additional noise reduction only leads to further improvement of the WTTD performance.

The housing of the motor modules and the power supplies of the WTTD, as well as the carriage for the sensor modules, is depicted in Figure B.1. However, the board and the housing for the sensor system might be reworked because the current photosensor needs a different positioning to measure anode wires above a cathode pad plane. The dimensions of the housing and the plate for the motoric and sensoric components are additionally given in Figures B.3, B.4 and B.5.

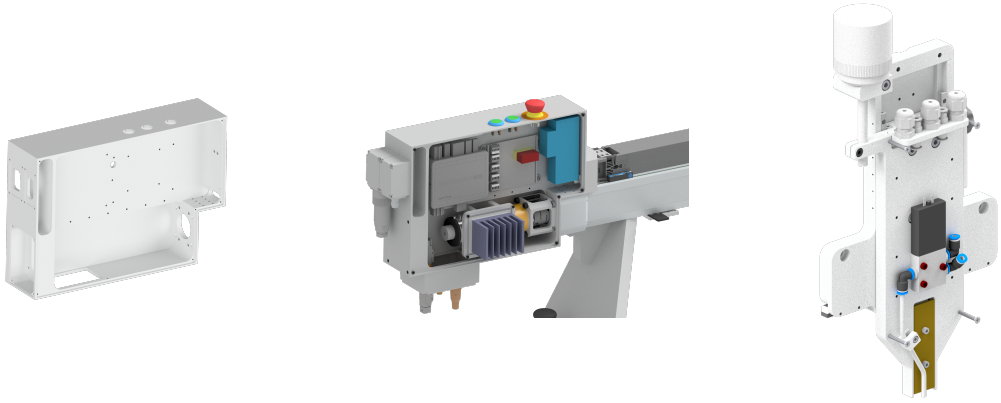

Figure B.1: Housing of the motoric components without (left) and with (center) the components. Included are the motion controller, the motor, the threaded spindle as well as the voltage supplies for each component. Note that the case is open and will be closed in later installation. On the right is the board for the sensoric components and the air pressure valve.

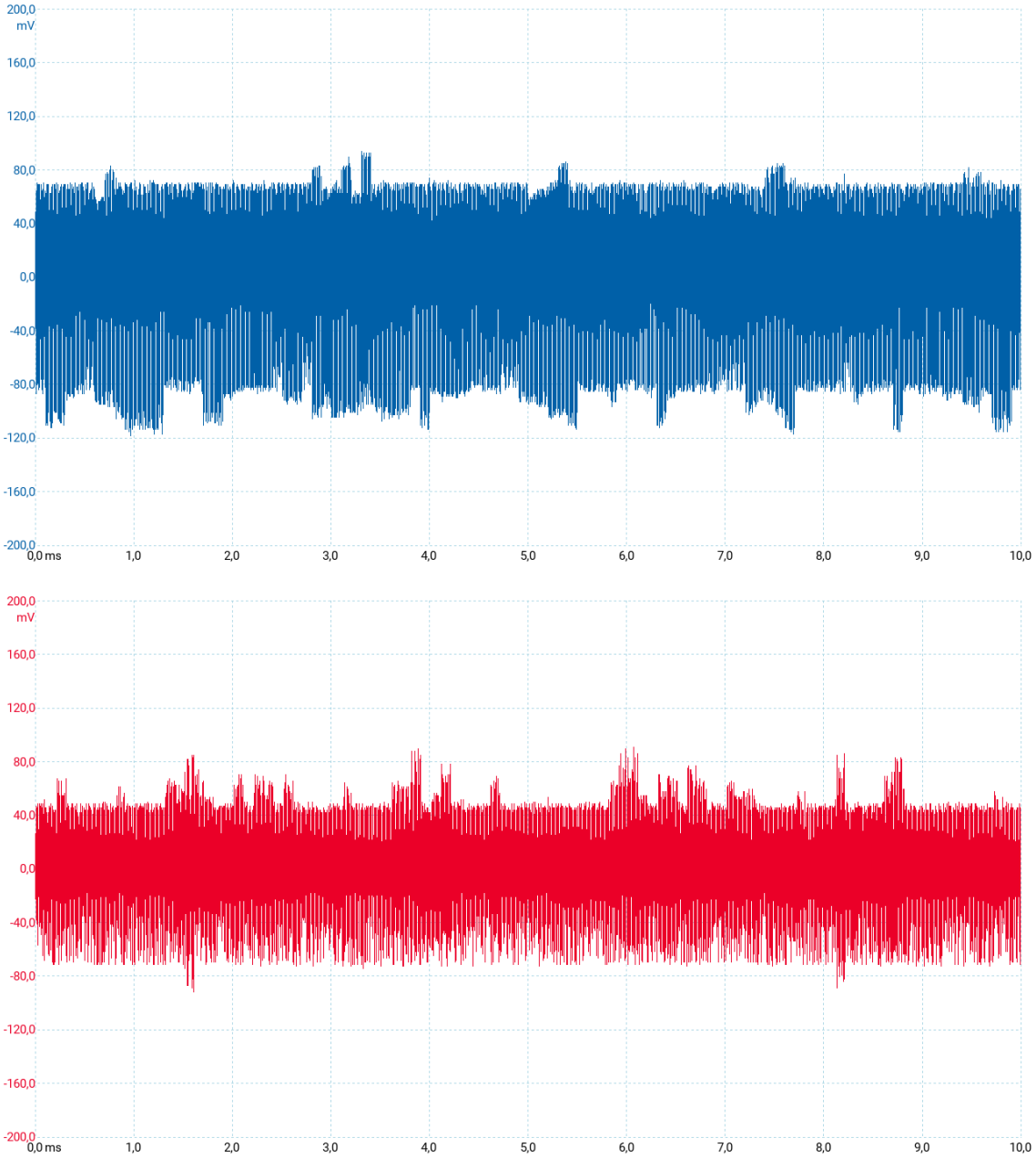

Figure B.2: Raw noise signal (top, blue) and amplified noise signal (red) while the motor moves the carriage. The raw noise signal is given with AC coupling and the amplified signal with DC coupling.

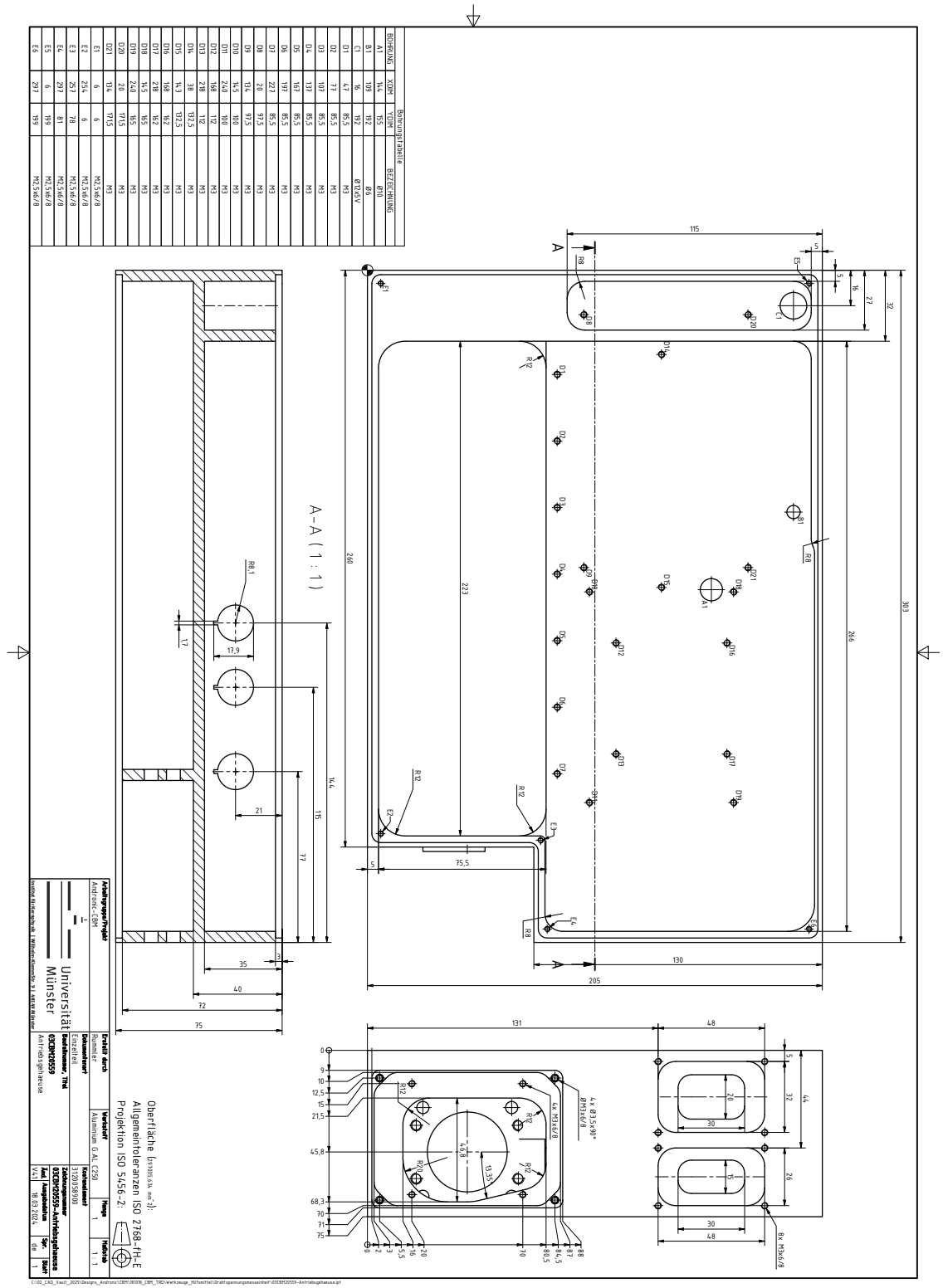

Figure B.3: Dimensioning of the housing case of the motoric components and the voltage supplies of the WTTD (page 1).

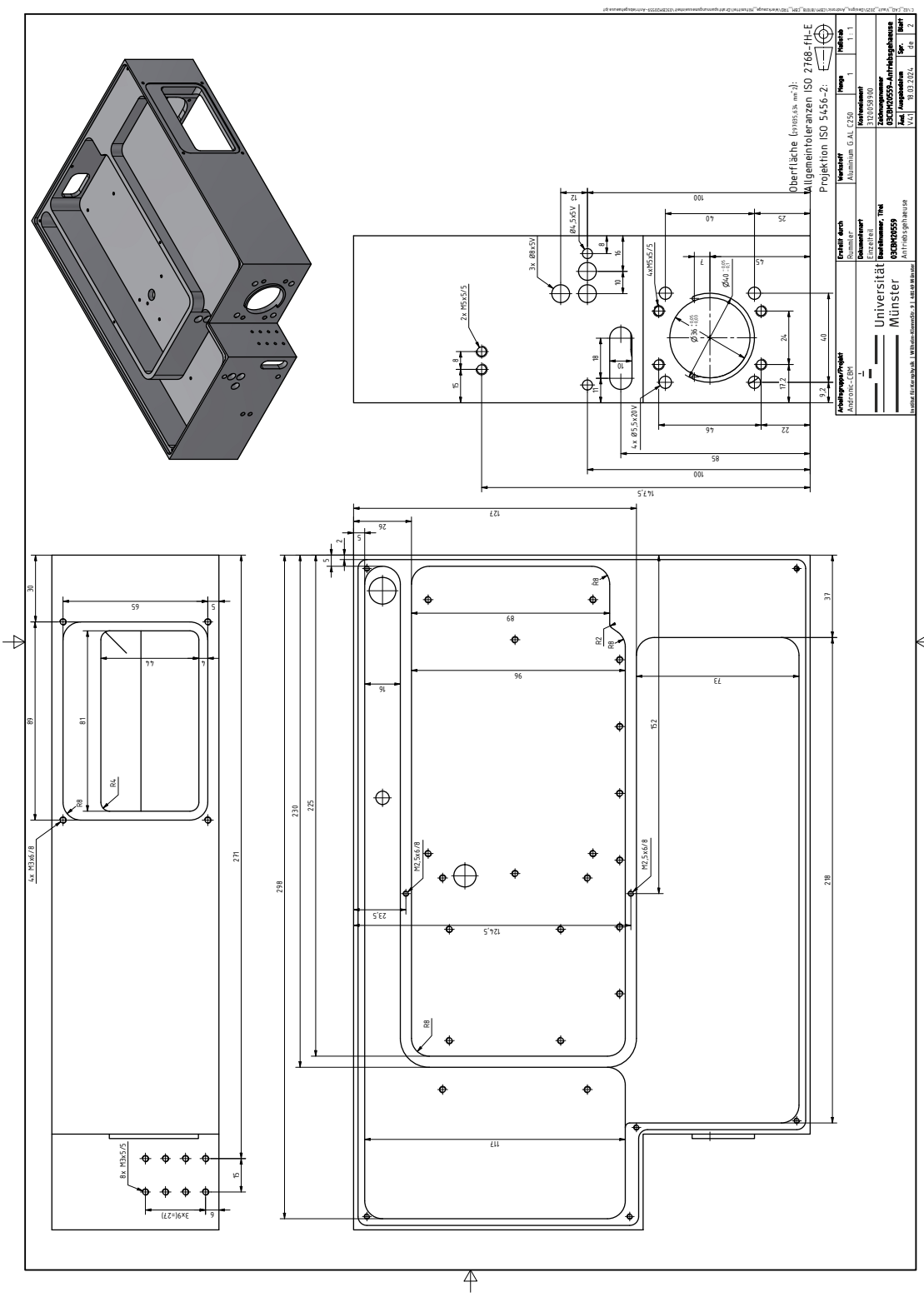

Figure B.4: Dimensioning of the housing case of the motoric components and the voltage supplies of the WTTD (page 2).

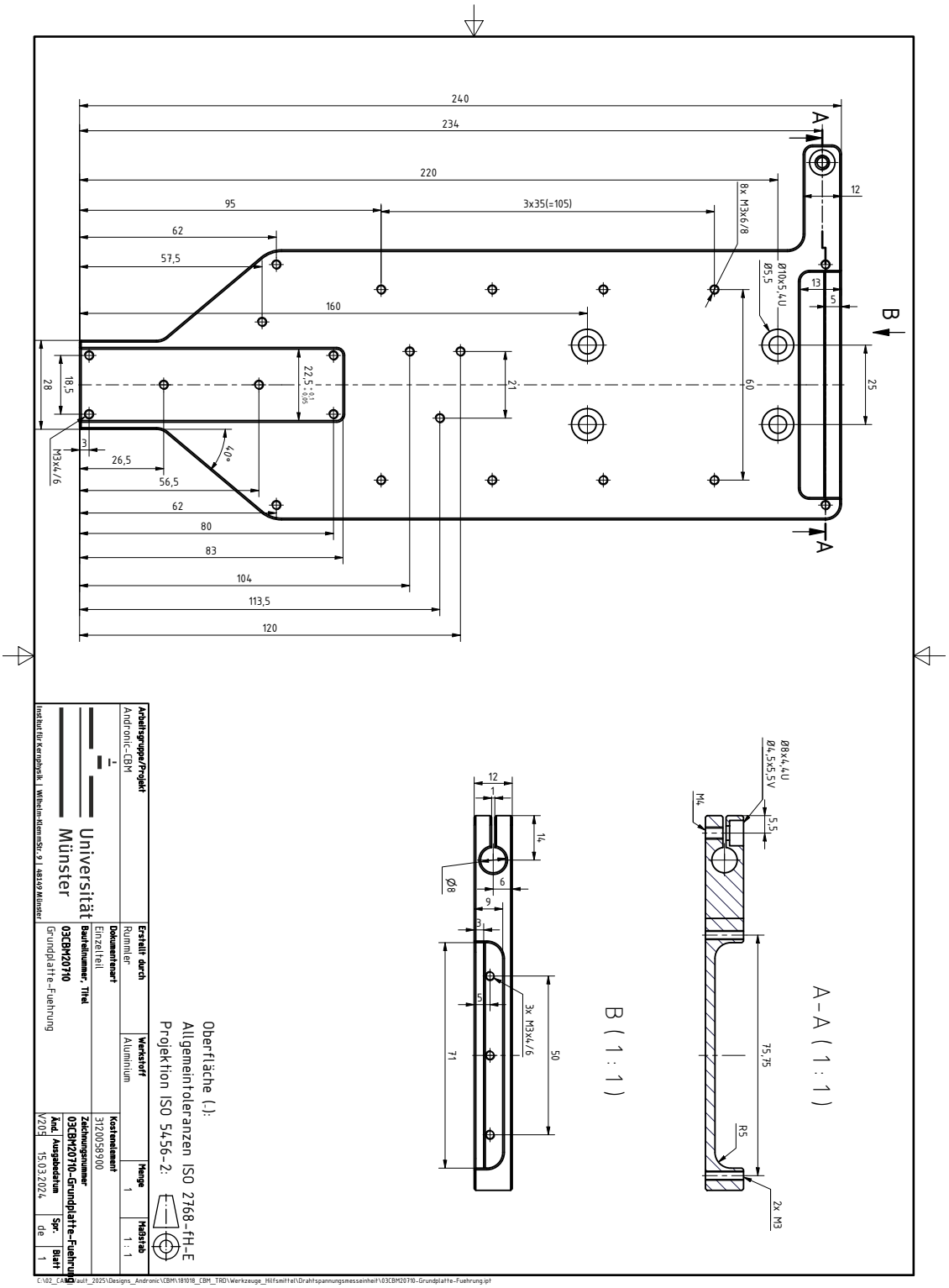

Figure B.5: Dimensioning of the board for the sensoric components of the WTTD.

Bibliography

[1] A. Bazavov *et al.* “The chiral and deconfinement aspects of the QCD transition”. Phys. Rev. D85:054503, 2012, arXiv: 1111.1710 [hep-lat].

[2] A. Schmah *et al.*, STAR Collaboration. “Highlights of the beam energy scan from STAR”. Central Eur. J. Phys. 10:1238–1241, 2012, arXiv: 1202.2389 [nucl-ex].

[3] BIPM *et al.* "Guide to the expression of uncertainty in measurement — Part 6: Developing and using measurement models". Joint Committee for Guides in Metrology, JCGM GUM-6, 2020, URL: https://www.bipm.org/utils/common/documents/jcgm/JCGM_GUM_6_2020.pdf, last visited: 09/02/2025, 10:33 p.m.

[4] CAN in Automation. "CAN: From physical layer to application layer and beyond". URL: https://www.can-cia.org/can-knowledge, last visited: 08/31/2025, 03:46 p.m.

[5] C. Blume *et al.*, CBM Collaboration. "The Transition Radiation Detector of the CBM Experiment at FAIR: Technical Design Report for the CBM Transition Radiation Detector (TRD)". Tech. rep. Collaboration FAIR, 2018, DOI: 10.15120/GSI-2018-01091.

[6] CBM Collaboration. "CBM Compressed Baryonic Matter experiment at FAIR". URL: https://www.cbm.gsi.de/projects, last visited: 08/27/2025, 04:13 p.m.

[7] C.E. Shannon. "Communication in the Presence of Noise". Proc. IRE. 37 (1), 1949, DOI: 10.1109/jrproc.1949.232969

[8] D. Blaschke et al., "Topical issue on exploring strongly interacting matter at high densities - NICA white paper". Eur. Phys. J. A 52 no. 8 (1), 2016, DOI: 10.1140/epja/i2016-16267-x.

[9] E. Macherauch and H.W. Zoch. Praktikum in Werkstoffkunde: 100 aus- führliche Versuche aus wichtigen Gebieten der Werkstofftechnik. Springer Fachmedien Wiesbaden, 2019. ISBN: 978-3-658-25374-5. DOI: 10.1007/978-3-658-25374-5_22.

[10] G.A. Erskine. "Electrostatic problems in multiwire proportional chambers". Nuclear Instruments and Methods 105.3 565-572, 1972, DOI: 10.1016/0029-554X(72)90356-4

[11] H. Gottschlag. "Entwicklung einer Apparatur zur automatisierten Positions- und Spannungsbestimmung von Drähten in Vieldrahtproportionalkammern". Universität Münster, Institut für Kernphysik, Feb. 2005.

[12] H. Hünteler. "Development and Evaluation of a Multiwire Proportional Chamber for a High Resolution Small Animal PET Scanner". Universität Münster, Institut für Kernphysik, Feb. 2007.

[13] H. Kolanoski and N. Wermes. "Teilchendetektoren: Grundlagen und Anwendungen". Springer, 2016. ISBN: 978-3-662-45350-6. DOI: 10.1007/978-3-662-45350-6.

[14] International Organization for Standardization and International Electrotechnical Commission. "Information technology — Open Systems Interconnection — Basic Reference Model: The Basic Model". ISO/IEC 7498-1, 1994, URL: https://www.iso.org/standard/20269.html, last visited: 09/02/2025, 10:35 p.m.

[15] J. Lämmel. "A Device for Measuring the Wire Tension of the MWPCs in the CBM TRD". Universität Münster, Institut für Kernphysik, Apr. 2024.

[16] J. Rafelski. "Connecting QGP-Heavy Ion Physics to the Early Universe". Nuclear Physics B - Proceedings Supplements, Nov. 2013, DOI: 10.1016j.nuclphysbps.2013.09.017.

[17] K. Fukushima and T. Hatsuda. "The phase diagram of dense QCD". Rept. Prog. Phys. 74:014001, 2011, arXiv: 1005.4814 [hep-ph].

[18] M. Esen. "Implementation of an Automated Position and Tension Determination of Wires in Multi-Wire Proportional Chambers". Göthe-Universität Frankfurt am Main, Institut für Kernphysik, Nov. 2018

[19] M. Falch. "CAN Bus - THe Ultimate Guide". CSS Electronics, 2022, URL: https://www.csselectronics.com/pages/can-bus-ultimate-guide, last visited: 09/02/2025, 10:36 p.m.

[20] MicroControl Systemhaus für Automatisierung. "Transmitter - Manual for transmitter modules". 2024, URL: https://files.microcontrol.net/manual/hb_mcan_trs_v2r00_en.pdf, last visited: 09/02/2025, 10:37 p.m.

[21] N. Herrmann, CBM Collaboration. "Status and Perspectives of the CBM experiment at FAIR". EPJ Web Conf. Volume 259, 2022, DOI: 10.1051/epjconf/202225909001

[22] O. Pfeiffer *et al.* "Embedded Networking with CAN and CANopen". Copperhill Technologies Corporation, 2003. ISBN: 978-0-9765116-2-5.

[23] P.A. Tipler *et al.* "Tipler Physik". Springer Verlag, 2024, ISBN: 978-3-662-67935-7, DOI: 10.1007/978-3-662-67936-4

[24] P.A. Zyla *et al.* "2020 Review of Particle Physics". Particle Data Group, Prog. Theor. Exp. Phys. 2020, 083C01, 2020, URL: https://pdg.lbl.gov/2020/tables/contents_tables.html, last visited: 09/02/2025, 10:41 p.m.

[25] S. Acharya *et al.*, ALICE Collaboration. "The ALICE experiment: a journey through QCD". Eur. Phys. J. C 84:813, 2024, arXiv: 2211.04384 [nucl-ex].

[26] S.J. Ling *et al.* "University Physics Volume 1". OpenStax, Rice University, 2016, ISBN: 978-1-938168-27-7

[27] W.H. Press *et al.* "Numerical Recipes - The Art of Scientific Computing". Cambridge University Press, 2007, ISBN: 978-0-521-88068-8

[28] W. Kester. "MT-002 Tutorial What the Nyquist Criterion Means to Your Sampled Data System Design". ResearchGate, Analog Devices, Inc., 2016, URL: https://www.researchgate.net/publication/265323668_MT-002_TUTORIAL_What_the_Nyquist_Criterion_Means_to_Your_Sampled_Data_System_Design, last visited: 09/02/2025, 10:44 p.m.

Acknowledgement

In the end, I would like to take this opportunity to thank and appreciate everyone who supported me during the creation of this bachelor thesis.
First, I want to thank every member of the working group AG Andronic. Be it the lunch breaks with the highly competitive nerd quiz, the spontaneous language lessons in the office, or other occasions like bicycle trips, barbecues and parties, you all made my daily life during this period exciting and I really enjoyed sharing each moment with you.
Special thanks go out to the CBM members of the working group who not only introduced me to the CBM experiment, but also made it possible for me to join the 45th CBM collaboration meeting. I got interesting insights into the research of particle physics and met many kind and motivated people.
I also want to express my appreciation to Roland Berendes, who created the preamplifier and the low-pass filter for the sensor system, as well as Daniel Bonaventura, who provided me with the CAD render of the WTTD.
I want to thank Johannes Lämmel for his great work on the WTTD and the precise documentation within his bachelor thesis, as it contributed a lot to my understanding of the working principles of the WTTD.
Furthermore, I would like to express my deep gratitude to Philipp Kähler for erasing my doubts, answering my numerous questions, helping me in the laboratory and improving my scientific writing skills.
Lastly, I want to sincerely thank my professors and examiners Anton Andronic and Christian Klein-Bösing, who gave me the opportunity to be part of this research group in the first place. It was a great experience and I will enjoy remembering this time.